

Chemical templates that assemble the metal superhydrides

*Yuanhui Sun and Maosheng Miao**

Department of Chemistry and Biochemistry, California State University Northridge, CA USA

*Email: mmiao@csun.edu

The recent discoveries of many metal superhydrides provide a new route to room temperature superconductors. However, their stability and structure trends and the large chemical driving force needed to dissociate H₂ molecules and form H covalent network cannot be explained by direct metal-hydrogen bonds and volume effect. Here, we demonstrate that the understanding of superhydrides formation needs a perspective beyond traditional chemical bond theory. Using high-throughput calculations, we show that, after removing H atoms, the remaining metal lattices exhibit large electron localizations at the interstitial regions, which matches excellently to the H lattice like a template. Furthermore, H lattices consist of 3D aromatic building units that are greatly stabilized by chemical templates of metals close to s-d border. The chemical template theory can naturally explain the stability and structure trends of superhydrides and help predicting new materials such as two-metal superhydrides.

Among many remarkable physical and chemical properties of hydrogen, its capability of achieving superconducting state at or above room temperature has received intensive attention in condensed matter studies for many decades.¹⁻³ However, hydrogen is very resistive to metallization and polymerization that is an essential step toward superconductivity, and large driving forces are needed to overcome it. As predicted theoretically, a tremendous high pressure of 550 GPa is needed to drive the transformation of hydrogen to atomic phases.^{1,4,5} Therefore, the chemical forces that can “pre-compress” the hydrogen became an attractive approach of superconductive hydrogen under moderate pressure² and have led to the predictions and syntheses of numerous hydrogen-rich compounds that brought us ever close to room temperature superconductivity.^{6,7} These compounds can be roughly categorized into metal hydrides and non-metal hydrides. As the second type of hydrides, H₃S showed a T_c of 203 K near 150 GPa,⁸ which is the first to break the 25-year T_c record of cuprates. More profoundly, a ternary C-S-H system has just been demonstrated to become superconducting at about 15 °C and 267 GPa.⁹ All H atoms in these compounds bond with p-block elements that are in hypervalent states.¹⁰ In contrast, many metals close to the s-d border such as Ca, Sc, Y, La, Ce, Th incline to form superhydrides with exceedingly high H compositions in which all H atoms form extended lattices (Fig. 1a-c).¹¹⁻¹⁸ The H lattices in these compounds feature strong covalent H-H bonding, high electron density and strong electron-phonon coupling, giving rise to superconductivity at very high temperatures.¹⁹⁻²¹

A large chemical driving force is needed to explain the formation of metal superhydrides. The available assumptions focus either at the volume effect or charge transfer between metals and hydrogen,^{7,11} which can be examined by splitting the enthalpy changes into the changes of internal energy and the PV term (Fig. 1d-f and Supplementary Fig. 1). Generally, metallic hydrogen phases such as Cs-IV^{22,23} show significant volume reduction while comparing with molecular phases such as C₂/c^{24,25}, but their internal energies are much higher at lower pressures. The volume reductions are even more significant for many superhydrides. However, for most of the superhydrides, ΔPV increases with pressure. The volume of H (as defined in methods section) in LaH₁₀ becomes higher than Cs-IV H at about 170 GPa and even higher than molecular C₂/c phase at about 330 GPa (Fig. 1f). Therefore, it cannot be a consistent driving force for the formation of superhydrides. The volume reduction of superhydrides at lower pressures is more of a result of strong chemical interactions with high symmetry constrains.

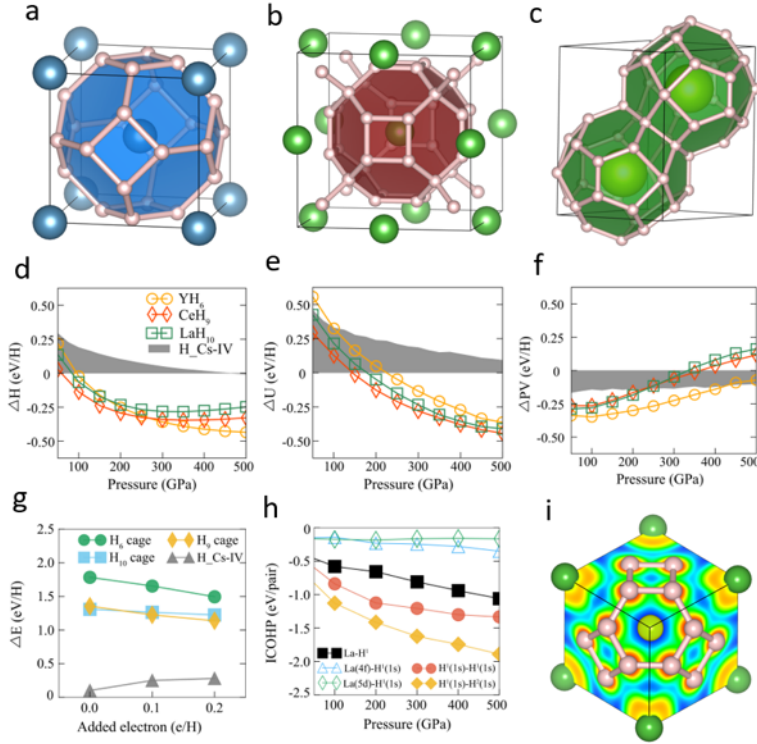


Fig. 1 | Structure, stability and bonding features of metal superhydrides. a – c. The sodalite structures of three major types of metal superhydrides, including CaH_6 in $Im\bar{3}m$ structure, LaH_{10} in $Fm\bar{3}m$ structure, and CeH_9 in $P6_3/mmc$ structure. The large blue, green and yellow balls represent the Ca, La, and Ce atoms; and the small white balls represent the H atoms. **d. – f.** The extracted enthalpy (ΔH), internal energy (ΔU) and ΔPV term of hydrogen in superhydrides relative to pristine hydrogen in molecular phase as functions of pressure (see Methods). The shaded areas show ΔH , ΔU , and ΔPV of metallic H in Cs-IV structure. **g.** The internal energies of hydrogen lattices (after removing metal atoms from superhydrides) in CaH_6 , LaH_{10} , and CeH_9 and of metallic hydrogen in Cs-IV structure relative to molecular hydrogen phase as functions of added charges. **h.** The integrated crystalline orbital Hamiltonian population (ICOHP) of La–H, La 5d – H¹ 1s, La 4f – H¹ 1s, H¹ – H¹, and H¹ – H² as functions of pressure. **i.** The electron localization function (ELF) of YH_6 at 300 GPa, viewed from (111) direction. A [111] cutoff plane is placed at a distance of 4.40 Å from the origin.

In contrast to PV, the relative internal energies of superhydrides decrease steadily while comparing with molecular and atomic hydrogen phases (Fig. 1e and Supplementary Fig. 1), indicating strong chemical interactions between H and metals. Electron doping theory attributes this chemical interaction to the charge doping from metals to H, which seemingly explains the destabilization of H₂ molecules because the extra electrons will occupy their anti-bonding states. However, calculations show that the excess charges also destabilize extended H lattices and the overall effect to H polymerization is insignificant (Fig. 1g). The energy of Cs-IV phase of metallic H actually goes up comparing with H₂ C₂/c phase while adding electrons (Fig. 1g). Furthermore, the charge doping from metal to hydrogen in superhydrides decreases with increasing pressure, distinctly opposing the trend of internal energy. Besides charge doping, the strong covalent bonding between metals and hydrogen seems to be another candidate of the driving force. However, both integrated Crystalline Orbital Hamiltonian Population (ICOHP)²⁶ (Fig. 1h) and Electron Localization

Function (ELF)²⁷ (Fig. 1i) reveal that the M-H bond strengths are significantly weaker than H-H bonds and therefore can hardly cause the formation of extended H lattice. Especially, the very small ICOHP values between the 5d/4f orbitals of La and H 1s show that these orbitals do not play major roles in forming metal superhydrides.

A new set of questions emerged after putting together all the recently predicted and synthesized metal superhydrides. Several different structures are often found for superhydrides with same H compositions and their energy order strongly depends on metals. Although, the hydrogen lattices in these structures show intricate geometry, the metal atoms usually form simple lattices such as face-centered cubic (FCC), hexagonal close pack (HCP), simple hexagonal etc., or lattices slightly deformed from them. For example, most of the MH₉ except PrH₉ and PaH₉, adopt hexagonal structures in which the metal atoms form HCP or SH lattices. Also, the MH₁₂ structure with highest symmetry (*Fm* $\bar{3}$ *m*) consists of FCC metal lattice and H cubo-octahedra locating at the octahedral sites. However, BaH₁₂ in this structure is significantly higher in energy than a distorted structure with P2₁ symmetry, although the Ba lattice in the latter structure forms a slightly distorted FCC lattice.²⁸ The stability trend of these structures is hard to be explained by the direct chemical interactions between metals and H.

In the following sections, we will show that instead of directly bonding with H, the presence of the metals significantly enhances the stability of the extended hydrogen lattices in superhydrides through a chemical template effect. The new theory can explain the formation of the superhydrides, the trend of metals that can form superhydrides across the periodic table, the preferences of superhydride structures for different metals, etc. It can also help to search new superhydrides, especially those with higher H compositions and with mixed metals.

Results and discussions

The electron localizations in metal lattices. The first step toward the mechanism of superhydrides formation is noticing that the electron localizations are ubiquitous in metals including the metal sub-lattices of superhydrides. In high-pressure electrides (HPE) such as hP4 Na, electrons occupy the local quantum orbitals at the interstitial site and play the role of anions of ionic compounds.^{29,30} This view can be extrapolated to many low-pressure structures of metals in which electrons only partially occupy the interstitial orbitals, rendering them in metallic states. For example, the La atoms in LaH₁₀ at 300 GPa correspond to a face-centered cubic (FCC) lattice at 12.4 GPa. Its ELF exhibits maxima with considerable values of 0.62 and 0.45 at the centers of octahedral (E^O) and tetrahedral (E^T) sites, suggesting some crystal orbitals have large distributions at these areas (Fig. 2a). As a matter of fact, the three highest occupied crystal orbitals (CO) at the Γ point that are 2.96 (HOMO-2), 2.38 (HOMO-1) and 2.33 (HOMO) eV below E_F, show maxima and large contributions at E^O sites, both E^O and E^T sites, and E^T sites, respectively (Fig. 2b-d). On the other hand, the charge distribution of FCC La shows no maxima at E^O and E^T sites; therefore, it is not an HPE. Similar localizations also happen to other metal lattices, for example, Sc BCC lattice in ScH₆ (Fig. 2e) and Y HCP lattice in YH₉ (Fig. 2f).

The strengths and the sites of the electron localizations strongly depend on the metal atoms and the geometry, and they evolve systematically with the size of the metal lattices. While lattice constant reduces, the general trend of the electron localization is from sites with less to sites with more surrounding atoms (Fig. 2g-h). For example, while the unit length of an FCC Ca lattice reduces, the electron localization shifts from sites between two atoms (bond center), to E^T sites, and then to E^O sites (Fig. 2i-j). For metals in the same period, the electron localization decreases with increasing atomic number. They are the strongest for s-block metals and early transition metals and become much weaker for late transition and p-block metals such as Al (Fig. 2k-n). Interestingly, the localizations for early transition metals such as Y, La, and Hf etc. are strong on both E^O and E^T sites, an important feature that will stabilize MH₁₀ superhydrides. It is important to notice the difference between the electron localizations and electron distributions at the interstitial sites. Metals like Al cannot stabilize H lattice and form superhydrides, although they have very high electron densities at the interstitial sites.

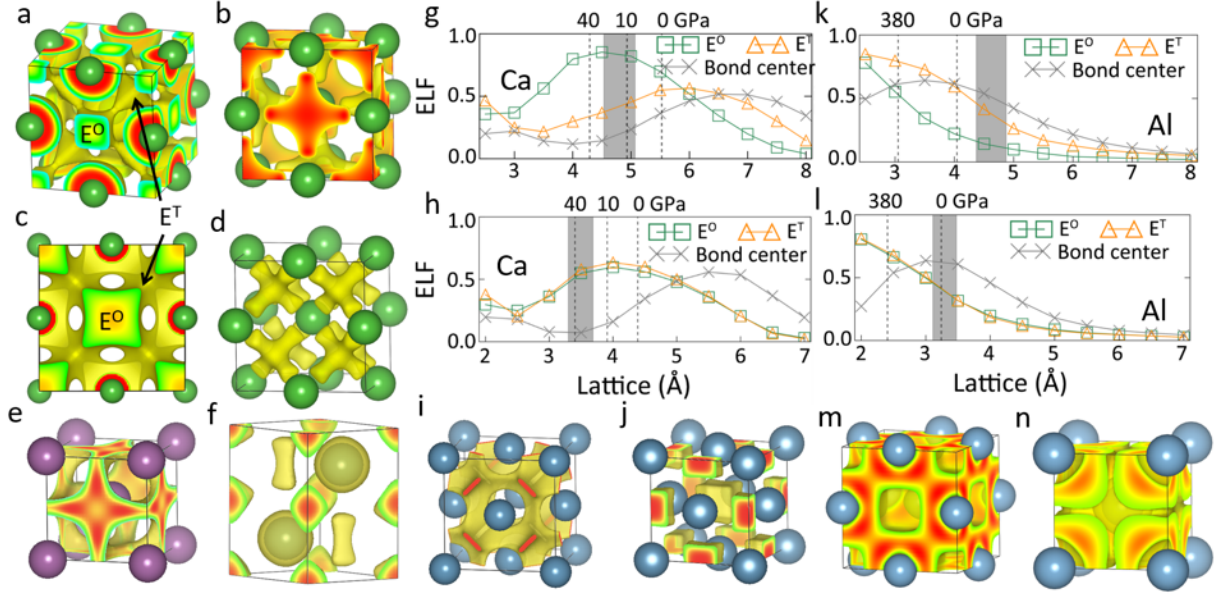


Fig. 2 | The electron localizations and their evolutions in metal lattices. **a.** The ELF of La sublattice in LaH₁₀ at 300 GPa. **b. – d.** Crystal orbitals HOMO, HOMO-1, and HOMO-2 at the Γ point of La sublattice in LaH₁₀. **e.** The ELF of Sc BCC lattice in ScH₆ at 100 GPa. **f.** The ELF of Y HCP lattice in YH₉ at 300 GPa. **g.** ELF values at interstitial sites in Ca FCC as functions of unit length. The shaded area shows the unit lengths of Ca lattice in a conceived CaH₁₀ at pressures from 100 to 300 GPa. **h.** ELF values at interstitial sites in Ca BCC as functions of unit length. The shaded area shows the unit lengths of Ca lattice in CaH₆ at pressures from 100 to 300 GPa. **i.** ELF of Ca FCC lattice with a unit length of 6.5 Å. At this length, FCC Ca show large electron localizations at E^T sites. **j.** ELF of Ca FCC lattice with a unit length of 4.7 Å. This length corresponds to Ca FCC lattice in a conceived CaH₁₀ under 300 GPa. **k.** ELF values at interstitial sites in Al FCC as functions of unit length. The shaded area shows the unit lengths of Al lattice in a conceived AlH₁₀ at pressures from 100 to 300 GPa. **l.** ELF values at interstitial sites in Al BCC as functions of unit length. The shaded area shows the unit lengths of Al lattice in a conceived AlH₆ at pressures from 100 to 300 GPa. **m.** ELF of Al FCC lattice under ambient pressure. **n.** ELF of Al BCC lattice under ambient pressure. Both ELF's show that electrons in Al lattices localize mainly around Al atoms due to the occupation of Al orbitals.

The building units of H lattices. The second key feature of superhydrides is that the H lattices consist of unique and intrinsic building units (Fig. 3a) that are positioned right at the active regions of the metal templates. They can be identified by the geometry, symmetry and the crystal orbitals of H lattices (Fig. 3b, c). Some units are straightforward to identify by their appearance in the lattice, such as H₆ hexagons and H₄ squares in MH₆, and H₈ cubes and H₅ tetrahedrons in MH₁₀; whereas some others are quite unexpected. For example, the H units in MH₉ are not H₅ and H₆ rings, but rather a H₆ corona and a H₈ bipyramid (Fig. 3a). These two units share most of the symmetries of MH₉, and many occupied crystal states localize on them (Fig. 3c). The ways that H lattices are divided into building units are also corroborated by their energies that are calculated by use of a He-matrix model (see Methods). Among the 6 building units in MH₆, MH₉ and MH₁₀, the H₆ hexagon, the H₈ cube and the H₆ corona are significantly lower in energy. Also, their energies decrease for about 0.5 eV/atom while pressure increases from 100 GPa to 300 GPa (Fig. 3d).

The remarkable stability of H₆ hexagon, H₈ cube and H₆ corona originates from an important feature of H-H bond. Due to the quantum resonance, these bonds are conjugated and delocalized in the same way as the C-C 2p π bonds in organic molecules of which the stability is ruled by the aromaticity.^{31,32} Because of the topology of the π bonds, the aromatic molecules need to assume a planar geometry and their electron counting needs to satisfy 4n+2 rule, which ensures a gap between the fully occupied and unoccupied orbitals. However, in contrast to C π bonds, the conjugation of H-H bonds is not constrained inside the same plane. The corresponding three-dimensional aromaticity depends on the symmetry and the number of H in the cluster, and the above three H clusters are all aromatic. The energy levels of H₆ hexagon resemble the energy levels of the benzene ring,³¹ and the highest occupied (HOMO) and the lowest unoccupied molecular orbitals (LUMO) are doubly degenerate (Fig. 3e). In contrast, the HOMO and LUMO of H₈ cube are triply degenerate (Fig. 3f). The HOMO-LUMO gaps of H₆ hexagon, H₈ cube and H₆ corona are 8.50, 10.15 and 7.77 eV, respectively. Many other aromatic H clusters are also identified as building units in various superhydrides (Supplementary Section II).

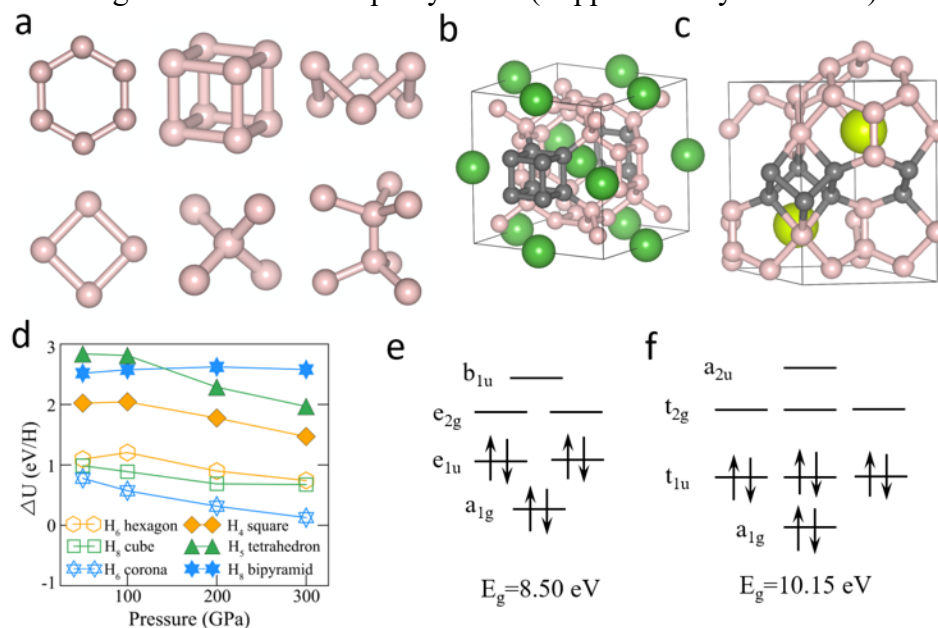


Fig. 3 | The building units of H lattices in superhydrides. **a.** The six building units of the H lattices in MH₆, MH₁₀ and MH₉ superhydrides, including the H₆ hexagon, the H₄ square, the H₈ cube, the H₅ tetrahedron, the H₆ corona and the H₈ bipyramid. **b.** The H₈ cube, a building unit of H₁₀ lattice in LaH₁₀. **c.** The H₆ corona, a building unit of H₉ lattice in CeH₉. **d.** The energies of the H units relative to H₂ molecules as functions of pressure. The calculations are performed by use of the He matrix model. **e.** The symmetries and the calculated energy levels of a H₆ hexagon. **f.** The symmetries and the calculated energy levels of a H₈ cube.

The assembly of H covalent network on metal templates. While the ELF and the COs of metal sublattices in superhydrides are overlaid on the corresponding H lattices, a striking feature of the superhydrides emerges unexpectedly. The H lattice matches excellently with the ELFs (Fig. 4a-c) and relative COs (Fig. 4d) of the metal lattices that include no information of H atoms at all. The H₁₀ lattice in LaH₁₀ consists of two types of H, H^I that forms H₈ cubes locating at the E^O sites, and H^{II} locating at E^T sites. Furthermore, some COs of the H₁₀ lattice also consist of orbitals locating

at E^O and E^T sites. At Γ point, the lowest unoccupied CO (Fig. 4e) consists of orbitals locating at both E^O and E^T . Therefore, while the La and the H_{10} lattices are interposed together, the occupation of E^O and E^T orbitals in La valence bands will naturally dope H_{10} by occupying its conduction band states. Indeed, the highest occupied state of LaH_{10} at the Γ point consists of orbitals at E^O and E^T (Fig. 4f). Therefore, instead of direct charge transfer from La atoms to H atoms, large part of the electron density of La lattice already localizes around the consisting motifs of H lattices, forming a chemical template awaiting and assisting the assembly of the H lattice.

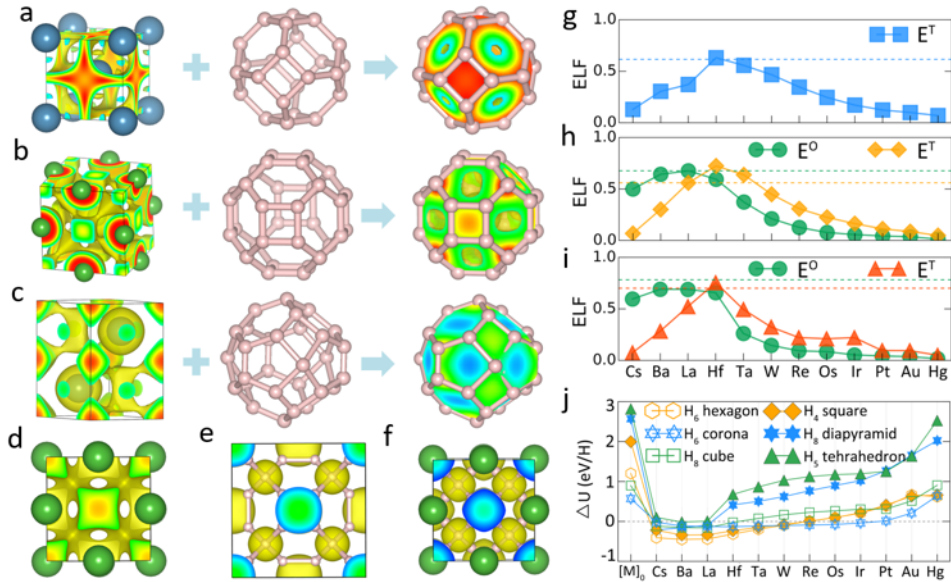


Fig. 4 | Assemble H lattices in metal templates. **a.** The ELF of a Ca BCC lattice overlaid on H_6 lattice. **b.** The ELF of La lattice in LaH_{10} at 300 GPa, overlaid on the H_{10} lattice. **c.** The ELF of Ce lattice in CeH_9 at 300 GPa, overlaid on the H_9 lattice. **d.** The density distribution of state HOMO-1 at Γ point of La lattice in LaH_{10} at 300 GPa. **e.** The density distribution of the lowest unoccupied state (LUMO) at Γ point of the H_{10} lattice (after removing La atoms) in LaH_{10} at 300 GPa. **f.** The density distribution of the highest occupied state (HOMO) of LaH_{10} at Γ point at 300 GPa. **g.** The ELF values at E^T sites of 6th row metal BCC lattice with a unit length corresponds to MH_6 at 100 GPa. The dashed line corresponds to the value at E^T site of Ca BCC lattice in CaH_6 . **h.** The ELF values at E^O and E^T sites of 6th row metal FCC lattice with a unit length corresponds to MH_{10} at 100 GPa. The dashed lines correspond to the values at E^O and E^T sites of La FCC lattice in LaH_{10} . **i.** The ELF values at E^O and E^T sites of 6th row metal HCP lattice with a unit length corresponds to MH_9 at 100 GPa. The dashed lines correspond to the values at E^O and E^T sites of Ce HCP lattice in CeH_9 . **j.** The energies of the H units relative to H_2 with the presence of metals in the 6th row of periodic table, calculated by use of the He matrix at 100 GPa.

The close match of the metal ELF and the H lattice is found for all metal superhydrides despite the large variation of structures and symmetries, such as MH_6 in $Im\bar{3}m$ structure (M= Sc, Ca, Y), MH_9 in $P6_3/mmc$ structure (M=Ce, Pr, La, etc.), MH_{10} in $P6_3/mmc$ structure (M=Y, Ac, etc), MH_{12} in $Fm\bar{3}m$ structure (M= Ba) and MH_{16} in $P6/mmm$ structure (M=La, etc.) and many others (Fig. 4g-i and Supplementary Section III). The metals in these superhydrides may adopt many different structures, including FCC, body-center cubic (BCC), hexagonal close-packed (HCP), simple cubic (SC), simple hexagonal (SH), or structures that deformed along high symmetry directions of them.

These sub-lattices are not necessary the stable structures of metals. Especially, for non-cubic superhydrides, the stresses of the metal lattices are usually not hydrostatic (Supplementary Table 3). For example, the normal stresses of the Ce lattice in CeH₉ at 300 GPa are $\sigma_1=\sigma_2=1.1$ GPa, $\sigma_3=15.1$ GPa. Nevertheless, all metal lattices show large electron distributions in the interstitial regions that match nicely with the locations and patterns of the H lattices in superhydrides, even if many superhydrides are in low symmetry structures, such as $R\bar{3}m$ SrH₆ and $Immm$ Ti₂H₁₃ and the corresponding ELF and H lattices exhibit complicated geometry features. On the other hand, the strength of the template effect that can be estimated by the ELF values at the interstitial sites strongly depends on metals. While they are the strongest for metals at the s-d border, they decline quickly for metals away from that region and become insignificant for late transition metals (Supplementary Fig. 2). For example, in an FCC Ir lattice of a conceived IrH₁₀ compounds, the maxima of ELF are no longer at the interstitial sites but in the regions between neighboring Ir atoms.

The presence of the metal sub-lattices greatly improves the stability of H building units due to the chemical template effects and the strength of template as measured by ELF intensities strongly depend on the metal (Fig. 4g-i) as well as the pressure (unit length). We employ high throughput calculations using the He matrix model that allows comparing energies of H clusters with H₂ molecules in the same chemical environment (see Methods). The results show that the presence of the metal atoms can lower the energies of H units relative to H₂ for about 0.5 to 3 eV, including non-aromatic ones such as H₄ squares and H₅ tetrahedrons (Fig. 4j and Supplementary Fig. 3). This template effect strongly depends on metals. The most profound changes happen to the elements around the s-d border and decline with increasing number of d electrons, which is consistent with the trend of ELF (Fig. 4g-i and Supplementary Fig. 2). Among row 6 elements, those sit at the s-d border such as Ba and La can lower the energies of all H units except H₅ below H₂ at 300 GPa; whereas late transition metals such as Pt and Au show much weaker effect. Very few elements, including Ba, La and Th etc, could bring the energy of H₈ cube below H₂.

Pressure is essential to the stability of H lattice, by virtue of directly lowering the energies of H units and influencing the effect of metal templates. The distances between metal atoms are larger under lower pressure, reducing the electron density in the interstitial region and weakening the chemical driving force from the templates. The expansion of the metal lattices and the reduction of the template effect will also happen while more H atoms are packed into them, therefore placing limits to H compositions of superhydrides.

The chemical template theory. The conventional theory of chemical bonds in molecules and solid compounds take free atoms as the initial states.³³ The charge transfer and the bond energies are obtained by referring to free atoms and their quantum orbitals. While describing superhydrides MH_n, it is advantageous to take the sub-lattices, including metal and anion (H_n) lattices respectively, as the starting points. The Hamiltonian of compounds consisting of metals and anions can be written as $H = H_M + H_A$, in which H_M and H_A are the Hamiltonians of the metal and the anion sublattices. For ionic and largely polarized compounds, the valence states that are important for binding energy are more significantly determined by H_A , giving ground for treating the effects of metal lattices as a perturbation. Indeed, in highly ionic compounds, the valence states ψ_0 mainly consist of the local orbitals around the anions.

While using stationary perturbation theory and treating H_M as the perturbation, the energy change of the valence state ψ_0 due to the presence of the metal sublattice is

$$\Delta\varepsilon = \langle \psi_0 | H_M | \psi_0 \rangle. \quad (1)$$

Assuming ψ_M^i are the crystal orbitals of the metal sublattice, H_M can be expressed as

$$H_M = \sum_i \varepsilon_M^i |\psi_M^i\rangle \langle \psi_M^i|, \quad (2)$$

and consequently,

$$\Delta\varepsilon = \sum_i \varepsilon_M^i \langle \psi_0 | \psi_M^i \rangle^2. \quad (3)$$

If we assume only one crystal orbital of the metal sublattice ψ_M^1 has large overlap with ψ_0 , $\Delta\varepsilon \approx \varepsilon_M^1 \langle \psi_0 | \psi_M^1 \rangle^2$. Because $\varepsilon_M^1 < 0$, the large overlap integral $S_{0M} = \langle \psi_0 | \psi_M^1 \rangle$ will lower $\Delta\varepsilon$ and the valence state energy, and therefore will stabilize the compound. Therefore, the presence of the chemical template could significantly stabilize the compounds because it optimizes the electron distribution in both anion and cation sublattices.

The concept of chemical template provides a very different view to chemical bonds in solid compounds. The strong chemical interactions due to the template effect do not associate with large electron relocations, in contrast to both ionic and covalent bonds. The electron distributions in superhydrides are optimal not only to the whole compound but also to its consisting metal and H sub-lattices, which maximize the stability. Taking LaH₁₀ as an example, the summation of the density distributions of the sub-lattices $\rho(\text{La}+\text{H}_{10}) = \rho[\text{La lattice}] + \rho[\text{H}_{10}]$ resemble very nicely $\rho(\text{LaH}_{10})$ (Supplementary Fig. 4a), which can be seen more clearly by the fact that $\Delta\rho = \rho(\text{LaH}_{10}) - \rho(\text{La}+\text{H}_{10})$ is quite small. As a matter of fact, the integrated transferred charge calculated from $\Delta\rho$ is about -0.15e for La (Supplementary Fig. 4b), which is about 10 times smaller than the Bader charge calculated from $\rho(\text{LaH}_{10})$ (Supplementary Fig. 4c). The negative value indicates an electron transfer to La, which can be misinterpreted as the presence of anionic La,³⁴ while it is actually the transfer of a small portion of charges around E^O and E^T back to La.

Chemical templates in single-metal superhydrides. Chemical template theory not only can explain the formation of superhydrides but also can explain the energy order of different structures and guide the search of new superhydrides. After intense search of new superhydride compounds and structures in the past several years, it becomes clear that almost every MH_n composition corresponds to several structures with very different space groups. There is lack of a convincing and all-embracing theory explaining why different metals prefer certain structures. Many intricate structure preferences of superhydrides can be understood in the framework of chemical template theory. For example, between the two MH₉ structures^{13,18,35}, $P6_3/mmc$ (CeH₉) and $F\bar{4}3m$ (PrH₉), most metals prefer the former except PrH₉ and PaH₉ that are found in $F\bar{4}3m$ structure (Fig. 5a). In contrast to metals like Cs and Ba that show no significant electron localizations at E^O sites and to metals like Y and La that show strong localizations bridging E^T-E^T pairs (Fig. 5b), both features can lower the energy of $P6_3/mmc$ structure by relaxation in (111) direction, Pr and Pa show strong location at E^O site but no strong pair-bridging (Fig. 5c).

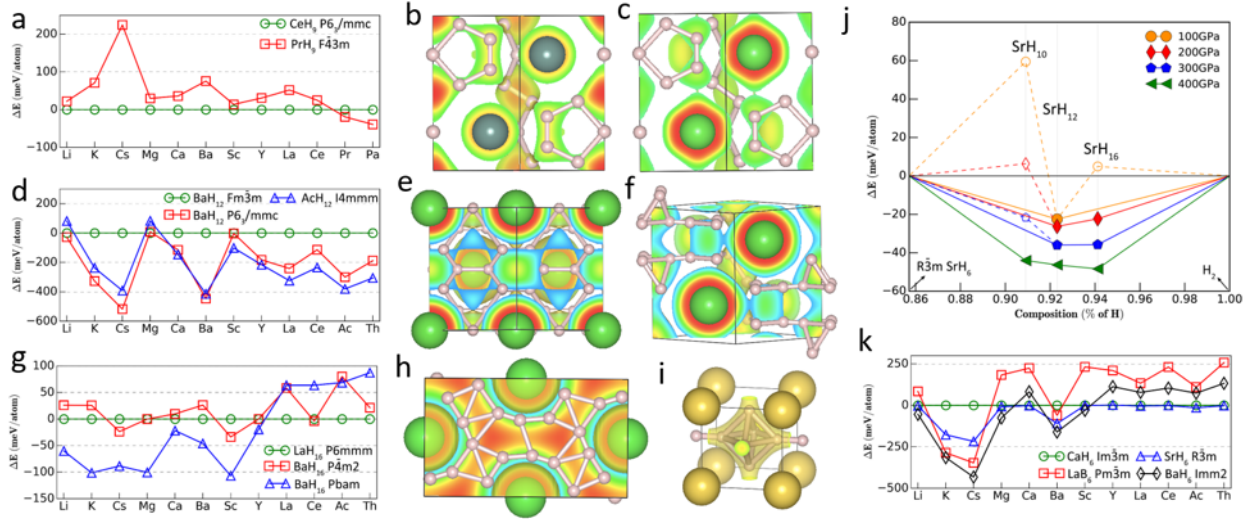


Fig. 5. The chemical templates and the structures of single-metal superhydrides. **a.** Structure preferences of MH_9 for selected metals. Two major structures, $P6_3/mmc$ and $F\bar{4}3m$ are compared. **b.** The ELF of Y sublattice in YH_9 in the $P6_3/mmc$ structure. **c.** The ELF of Pr sublattice in PrH_9 in the $P6_3/mmc$ structure. **d.** Structure preferences of MH_{12} of selected metals. **e.** The ELF of Ba sublattice in BaH_{12} in the $Fm\bar{3}m$ structure. **f.** The ELF of Ba sublattice in BaH_{12} in the $P6_3/mmc$ structure. **g.** Structure preferences of MH_{16} of selected metals. **h.** The ELF of Sr sublattice in SrH_{16} in the $Pbam$ structure. **i.** The ELF of Na sublattice in NaH_6 in the $Pm\bar{3}m$ structure (LaB_6). **j.** Partial convex hull of Sr-H superhydrides. SrH_6 is assumed to be stable throughout the pressure range. **k.** Structure preferences of MH_6 of selected metals.

In another example, the structure of BaH_{12} has been thoroughly studied by DFT based structure search method in conjunction with an experimental work. Among the predicted cubic structures that matches the X-ray diffraction pattern, the $Fm\bar{3}m$ BaH_{12} consists of highly symmetric H cubo-octahedra that occupy the E^O sites of FCC Ba. However, the energy of this structure is significantly higher than the distorted cubic structures such as the $P2_1$ and the $Cmc2_1$ structures²⁸ (Fig. 5d). The cause of this symmetry reduction is due to the less significant and yet considerable electron localization at the E^T sites that can be utilized to stabilize the H lattice in the structures with reduced symmetry (Fig. 5e). On the other hand, the HCP Ba lattice contains paired E^T sites and allow lower symmetry of the polyhedrons. The search of BaH_{12} superhydride structures by adding H atoms in the Ba HCP lattice found a $P6_3/mmc$ BaH_{12} structure (Fig. 5f) that is only 25 and 16 meV higher in energy than $P2_1$ BaH_{12} at 100 and 200 GPa, respectively. In case of several other metals, such as K and Cs, $P6_3/mmc$ is the most stable one among all known MH_{12} structures.

LaH_{16} is another promising structure with high H composition. La forms SH lattice in this structure and its ELF shows large electron localization at the prism interstitial sites (Fig. 5h). However, the ELFs of many other metals are distinctly different to La. Especially, there is lack of electron localization close to the metal hexagonal planes that are necessary to stabilize the LaH_{16} structure. We performed a crystal structure search for BaH_{16} and ScH_{16} by adding H atoms to Ba and Sc SH and SC lattices. Two MH_{16} structures are found including a new $Pbam$ structure containing an SH

metal lattice, and a $P\bar{4}m2$ structure containing a slightly deformed SC metal lattice. The latter structure has been found in a structure prediction study of AcH_n compounds under high pressure.³⁶ Although the identified $Pbam$ structure is lowest in energy for BaH_{16} , it is slightly above convex hull at pressures below 300 GPa, mainly due to the exceedingly stable BaH_{12} compound. However, after examining all other metals with strong template effect, we found that SrH_{16} in the same structure become stable at pressures above 186 GPa (Fig. 5j). HfH_{16} is also stable, but only at pressures below 110 GPa.

A large-scale structure search based on chemical templates might help us find more stable superhydrides. For example, the strong electron localization at the body center of the simple cubic lattice formed by alkali metals and Ba suggests possible superhydrides in LaB_6 structure. As a matter of fact, the MH_6 superhydrides of most alkali metals and Ba are more stable in LaB_6 structure than CaH_6 structure (Fig. 5k). However, in most of the cases except NaH_6 , their energies are slightly higher than BaH_6 $Imm2$ structure³⁷. Among all the known structures, NaH_6 is most stable in LaB_6 structure (Fig. 5i). While constructing the convex hull of Na-H binary compounds, NaH_6 is found to be 22 meV above the convex hull at 200 GPa.

Chemical templates in mixed-metal superhydrides. While almost all possible binary superhydrides have been tried out, the hope of achieving higher T_c at lower pressure rely on the search of novel ternary superhydrides composed of two different metals.^{12,38-41} Constructing a complete phase diagram of ternary superhydrides based on full-scale DFT calculations is extremely difficult, and the search of optimal compounds across the entire periodic table as we have done for binary superhydrides is an impossible task. To date, the diagrams of very few ternary superhydrides such as Li-Mg-H have been thoroughly searched, which predicted a metastable superhydride, Li_2MgH_{16} , that shows a T_c of $\sim 473K$ at 250 GPa.³⁸ The template theory allows us to assess the formation of mixed-metal superhydrides by studying only the metal lattices. High-throughput calculations show strong correlation between the enhancements of the template strength while mixing metals and the energy of formation of mixed metal superhydrides.

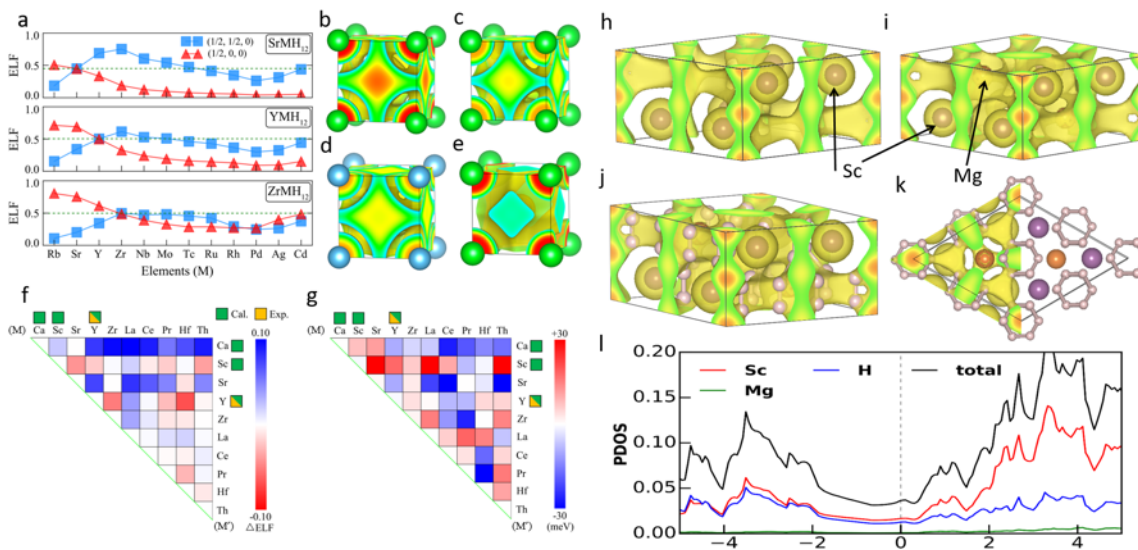


Fig. 6 | The chemical template effects in mixed-metal superhydrides. **a.** The ELF values of $MM'H_{12}$ mixed metal superhydrides at the interstitial points, including $(1/2, 1/2, 0)$ and $(1/2, 0, 0)$. M is Sr, Y and Zr, and M' is a 5th row metal element. **b. – e.** The ELF of $SrYH_{12}$, $SrZrH_{12}$,

YZrH₁₂ and SrAgH₁₂. **f.** The average ELF of MM'H₁₂ superhydrides at 100 GPa, $\Delta\text{ELF} = \text{ELF}_{\text{MM}'\text{H}_{12}}^{1/2,1/2,0} + \text{ELF}_{\text{MM}'\text{H}_{12}}^{1/2,0,0} - \text{ELF}_{\text{MH}_6} - \text{ELF}_{\text{M}'\text{H}_6}$, in which M and M' are Ca, Sc, Sr, Y, Zr, La, Ce, Pr, Hf and Th. **g.** The reaction enthalpy of forming MM'H₁₂, $\Delta H = (H(\text{MM}'\text{H}_{12}) - H(\text{MH}_6) - H(\text{M}'\text{H}_6))/14$, at 100 GPa. In both (**f**) and (**g**) the squats filled with green and orange colors show MH₆ superhydrides that are predicted by DFT calculations and synthesized by DAC experiments, respectively. **h.** ELF of Sc sublattice in Sc₃MgH₂₄ superhydrides. **i.** ELF of Sc₃Mg sublattice in Sc₃MgH₂₄ superhydrides. **j.** Side view of the ELF of Sc₃MgH₂₄ superhydrides. **k.** Top view of the ELF of Sc₃MgH₂₄ superhydrides. **l.** The total and projected density-of-states (DOS) of Sc₃MgH₂₄ superhydrides.

High throughput calculations based on the chemical template theory reveal two mechanisms of combining two metals to generate stable ternary superhydrides. In the first case, the combination of the two “template-active” metals might strengthen the effect. The ELF of two-metal lattices adapted from metal structures in MH₆, MH₁₀, and MH₉ at 100 GPa by partially replacing metal atoms (Fig. 6a-e and Supplementary Fig. 5) show the mixture with later transition metals greatly lowers the ELF values at the interstitial sites. In contrast, if both metals are close to s-d border such as Sr, Y and Zr (Fig. 6b-d), the resulting electron localization might be enhanced, which can be measured by $\Delta\text{ELF} = \text{ELF}_{\text{MM}'\text{H}_{12}}^{1/2,1/2,0} + \text{ELF}_{\text{MM}'\text{H}_{12}}^{1/2,0,0} - \text{ELF}_{\text{MH}_6} - \text{ELF}_{\text{M}'\text{H}_6}$ (Fig. 6f). More importantly, ΔELF shows strong correlation with the stability of the ternary superhydrides that is calculated as the reaction enthalpies $\Delta H = [H(\text{MM}'\text{H}_{12}) - H(\text{MH}_6) - H(\text{M}'\text{H}_6)]/14$ (Fig. 6g). For example, while mixing Sr and Y, the average ELF increases (Fig. 6b) and the SrYH₁₂ is stable against the decomposition into SrH₆ and YH₆ (Fig. 6g). In contrast, the mixture of Y and Zr leads to lower average ELF (Fig. 6c) and correspondingly YZrH₁₂ is not stable (Fig. 6g). Similar trend can be found for MH₉ and MH₁₀ related two-metal superhydrides (Supplementary Fig. 6). A rough estimation of T_c using the ratio of the density of hydrogen related states versus the total density of states⁴² at the Fermi level show that the mixing metals in superhydrides can potentially improve T_c (Supplementary Fig. 7).

In the second case, an active metal such as Li, Na and Mg etc. is mixed with a metal at the s-d border and enhance their template effect by doping electrons. For example, Sc₃Mg in *P6₃/mmc* structure show strong enhancement of the Sc template by adding Mg. The ELFs of the metal lattice with and without Mg show the same topology, but the values are significantly higher while adding Mg (Fig. 6h-i), which is caused by the electron transfer from Mg to Sc crystal orbitals. We thus conducted a structure search by adding H atoms into the Sc₃Mg metal lattice, which leads to the discovery of a superhydride Sc₃MgH₂₄ also in *P6₃/mmc* space group (Fig. 6j-k). This compound is stable against the decomposition into ScH₆, MgH₄ and H₂, with -0.54 meV/atom reaction enthalpy at 200 GPa. It shows considerable DOS at the Fermi level and might be a candidate superconductor under pressure (Fig. 6l). The results show that a large-scale study of the mixed metal lattices adapted from known intermetallic compounds and the change of their ELF is a promising and affordable approach to predicting mixed metal superhydrides in a massive scale. The mixed metal lattices adapted from MH₆, MH₁₀ and MH₉ in this work are also structures of known intermetallic compounds; and the Li-Mg lattice in Li₂MgH₁₆ is isostructural to Laves phase MgCu₁₂.³⁸

Conclusions

By studying the mechanism of metal superhydrides formation, we revealed a significant driving force of forming solid compounds that is not known before, *i.e.* the chemical template effect. Different to the traditional chemical bond theory that compares the compounds with free atoms, we view the formation of superhydrides as the interposition of metal and H sub-lattices. Our calculations showed large electron localizations at the interstitial sites due to the occupation of the crystal orbitals of the metal sublattices, forming chemical templates. They assist the dissociation of H₂ molecules and the formation of H covalent networks in superhydrides. Furthermore, the H sublattices consist of H building units that are aromatic despite that they are not planar. Calculations on a He-matrix model show that the presence of the metal sub-lattices can largely stabilize the building units of the H lattices. Furthermore, the chemical template theory explains the large structural variations and their energy orders for superhydrides with the same H composition. The potential of the chemical template mechanism in searching novel superhydrides especially with higher H compositions and mixed-metal are demonstrated. High-throughput calculations revealed a strong correlation between the strength of the chemical templates and the stability of the mixed metal superhydrides, indicating it can be used for a large-scale search of ternary and quaternary superhydrides. It will greatly enhance the efficiency of searching superhydride materials that might become superconducting at higher temperature and lower pressure.

Methods

Solid-state density functional calculations. The underlying first-principles density functional theory (DFT) calculations were carried out by using the plane-wave pseudopotential method as implemented in Vienna *ab initio* Simulation Package (VASP).^{43,44} The electron-ion interactions were described by the projector augmented wave pseudopotentials^{45,46} and the used valence electrons are listed in Table 1. Some calculations of late transition metals, such as the ELF trend of various lattices under compression are done using pseudopotentials without including the outer-core p orbitals in the valence. Our test calculations show that the differences caused by this choice of pseudopotentials is negligible. We used the generalized gradient approximation formulated by Perdew, Burke, and Ernzerhof⁴⁷ as exchange-correlation functional. A kinetic energy cutoff of 520 eV was adopted for wave-function expansion. The k -point meshes with interval smaller than $2\pi \times 0.03 \text{ \AA}^{-1}$ for electronic Brillouin zone to ensure that all enthalpy calculations converged within 0.02 eV/atom. The high-throughput first-principles calculations were performed by using the Jilin Artificial-intelligence aided Materials-design Integrated Package (JAMIP), which is an open-source artificial-intelligence-aided data-driven infrastructure designed purposely for computational materials informatics.⁴⁸

H											He
1s ¹											1s ²
K	Ca	Sc	Ti	V	Cr	Mn	Fe	Co	Ni	Cu	Zn
3s ² 3p ⁶ 4s ¹	3p ⁶ 4s ²	3s ² 3p ⁶ 3d ¹ 4s ²	3p ⁶ 3d ² 4s ²	3p ⁶ 3d ³ 4s ²	3p ⁶ 3d ⁵ 4s ¹	3p ⁶ 3d ⁵ 4s ²	3p ⁶ 3d ⁶ 4s ²	3p ⁶ 3d ⁷ 4s ²	3p ⁶ 3d ⁸ 4s ²	3p ⁶ 3d ¹⁰ 4s ¹	3p ⁶ 3d ¹⁰ 4s ²
Rb	Sr	Y	Zr	Nb	Mo	Tc	Ru	Rh	Pd	Ag	Cd
4s ² 4p ⁶ 5s ¹	4s ² 4p ⁶ 5s ²	4s ² 4p ⁶ 4d ¹ 5s ²	4s ² 4p ⁶ 4d ² 5s ²	4s ² 4p ⁶ 4d ³ 5s ²	4p ⁶ 4d ⁵ 5s ¹	4p ⁶ 4d ⁵ 5s ²	4p ⁶ 4d ⁶ 5s ²	4p ⁶ 4d ⁷ 5s ²	4p ⁶ 4d ⁸ 5s ²	4p ⁶ 4d ¹⁰ 5s ¹	4d ¹⁰ 5s ²
Cs	Ba	La	Hf	Ta	W	Re	Os	Ir	Pt	Au	Hg
5s ² 5p ⁶ 6s ¹	5s ² 5p ⁶ 6s ²	5s ² 5p ⁶ 5d ¹ 6s ²	5p ⁶ 5d ² 6s ²	5p ⁶ 5d ³ 6s ²	5p ⁶ 5d ⁵ 6s ¹	5p ⁶ 5d ⁵ 6s ²	5p ⁶ 5d ⁶ 6s ²	5d ⁷ 6s ²	5p ⁶ 5d ⁸ 6s ²	5d ¹⁰ 6s ¹	5d ¹⁰ 6s ²
		Ce	Pr	Ac	Th	Pa	U				
		5s ² 5p ⁶ 4f ¹ 5d ¹ 6s ²	5s ² 5p ⁶ 4f ³ 6s ²	6s ² 6p ⁶ 6d ¹ 7s	6s ² 6p ⁶ 6d ² 7s	6s ² 6p ⁶ 5f ² 6d ¹ 7s	6s ² 6p ⁶ 5f ³ 6d ¹ 7s				

Table 1. The valence configurations of the pseudopotentials used in our solid-state DFT calculations.

Energy analysis of H in superhydrides. In order to compare the energy terms, including the enthalpies, the internal energies and the PV terms, of the hydrogen in superhydrides directly with pristine hydrogen phases under pressure, we deduct the corresponding energies of the metal hydrides with typical composition, and refer it to those of C₂/c molecular H₂ phase. For example, the enthalpy H of the H incorporated into LaH₁₀ beyond its typical composition LaH₃ is calculated as $\Delta H(H) = [H(\text{LaH}_{10}) - H(\text{LaH}_3) - \frac{7}{2} \times H(\text{H}_2^{C2/c})]/7$. Similar formula is used to calculate $\Delta U(H)$ and $\Delta PV(H)$. These energy terms are used to compare with the corresponding values of pristine H phases, as shown in Fig. 1d-f and Supplementary Fig. 1.

Electronic structure Analyses of solid compounds. The electronic structures of metal superhydrides are calculated and analyzed by use of several methods, including the Bader's Quantum Theory of Atoms in Molecules (QTAIM),⁴⁹ the Electron Localization Function (ELF),²⁷ the Crystalline Orbital Hamiltonian Population (COHP) and integrated COHP (ICOHP),²⁶ and integrated differential charge density (see below), etc.

Integrated differential electron density. First, for a given metal superhydride (MH_n), three electron densities are calculated, including that of MH_n , of the metal lattice (MH_n after removing all H), and of the H lattice (MH_n after removing all metals). The differential electron density is then calculated as $\Delta\rho = \rho(MH_n) - \rho[\text{metal lattice}] - \rho[\text{H}_n \text{ lattice}]$. This differential density distribution is separated into regions by the surface(s) of $\Delta\rho=0$. Especially, all the metal atoms are surrounded by a surface of $\Delta\rho=0$ that is roughly spherical. In all the cases, $\Delta\rho>0$ inside the surface, indicating that electrons transfer toward metal atoms while interposing the metal and the H lattices. The total charge transfers to metals are calculated by integrating the differential electron density inside the $\Delta\rho=0$ surface. The charges shown in Supplementary Fig. 4c are negative because the electron charge is negative.

Quantum chemistry calculations on H clusters. The geometry parameters of all H clusters are adapted from the superhydrides optimized by solid-state DFT calculations at the studied pressures (100 and 300 GPa). Their molecular orbitals and the energy levels are calculated by using Gaussian 09 package.⁵⁰ The restricted open-shell B3LYP⁵¹⁻⁵³ and Hartree-Fock⁵⁴ methods are used for exchange and correlation functional for H cluster with even and odd number of H atoms respectively, respectively. The 6-31G(d) basis set is adopted for all the single-point calculations.

He matrix model. We build He matrix models to study the energies of various H clusters that are the building units of H lattices in superhydrides and compare them with H_2 molecules in the same chemical environment. Taking LaH_{10} as an example, we first optimize its structure to a selected pressure, for example 300 GPa. A supercell is constructed by triple the units in all three directions. After that, we replace all the H atoms with He atoms. By keeping or removing La metal atoms, we constructed two models, He_{320} and $La_{32}He_{320}$. The H clusters are created in these models by replacing corresponding He atoms with H atoms. For example, while modeling H_8 cubes, we replace 8 He atoms in a cube with H atoms. For comparison with H_2 molecules, we replace four pairs of He atoms in He_{320} and $La_{32}He_{320}$ by four pairs of H atoms. In order to compare the energies of H cluster with H_2 molecules at the same chemical environment, each H_2 molecule is placed at the sites that are part of H cluster. Also, the H_2 molecules are positioned to maximize their distances so to minimize the factitious H_2 - H_2 interactions in the model. The H coordinates in H_2 models are relaxed in order to maintain the lowest energy of H_2 molecules inside the He matrix. The relaxed H-H bond lengths in these models are close to that of H_2 molecules at ambient condition. The H atoms in the models of H clusters are not relaxed so that the H-H distances in these clusters are kept the same as in the H lattice of LaH_{10} at the studied pressure. Similarly, the supercell He-matrix models, including He_{96} and $Y_{16}He_{96}$, are constructed for YH_6 , and the energies of H_4 square and H_6 hexagon are studied using these models. The supercell He-matrix models, including He_{144} and $Ce_{16}He_{144}$, are constructed for CeH_9 , and the energies of H_6 corona and H_8 bipyramid are studied using them. In high-throughput calculations, metals in superhydrides vary, and the corresponding He-matrix model are created from the MH_n lattice optimized at the studied pressure.

Stability of mixed-metal superhydrides. The stability of the mixed-metal superhydrides is assessed by comparing their enthalpies with their constituent binary superhydrides. The enthalpy differences per atoms as shown in Supplementary Fig. 7 are calculated by the following formulae for three types of superhydrides based on $Im\bar{3}m$ MH₆, $P6_3/mmc$ MH₉ and $Fm\bar{3}m$ MH₁₀ superhydride structures. Specifically, the enthalpy differences are defined as:

$$\Delta H = (H(\text{MM}'\text{H}_{12}) - H(\text{MH}_6) - H(\text{M}'\text{H}_6))/14, \text{ for MM}'\text{H}_{12};$$

$$\Delta H = (H(\text{MM}'\text{H}_{18}) - H(\text{MH}_9) - H(\text{M}'\text{H}_9))/20, \text{ for MM}'\text{H}_{18};$$

$$\Delta H = (H(\text{M}_n\text{M}'_m\text{H}_{40}) - \frac{n}{4} \times H(\text{M}_4\text{H}_{40}) - \frac{m}{4} \times (H(\text{M}'_4\text{H}_{40}))/44, \text{ for M}_1\text{M}'_3\text{H}_{40}, \text{ and M}_3\text{M}'_1\text{H}_{40},$$

where $H(\text{MM}'\text{H}_{12})$, $H(\text{MH}_6)$, $H(\text{M}'\text{H}_6)$, $H(\text{MM}'\text{H}_{18})$, $H(\text{MH}_9)$, $H(\text{M}'\text{H}_9)$, $H(\text{M}_n\text{M}'_m\text{H}_{40})$, $H(\text{M}_4\text{H}_{40})$, and $H(\text{M}'_4\text{H}_{40})$ represents the enthalpies of ternary and binary superhydrides. Their structures are optimized at 100 and 300 GPa. M and M' represents the metals in 1-12 groups of 4-6 periods.

Data availability

The authors declare that all of the data supporting the findings of this study are available within the paper and the Supplementary Information, and also from the corresponding authors upon reasonable request.

References

1. Ashcroft, N. W. Metallic Hydrogen: A High-Temperature Superconductor? *Phys. Rev. Lett.* **21**, 1748–1749 (1968).
2. Ashcroft, N. W. Hydrogen Dominant Metallic Alloys: High Temperature Superconductors? *Phys. Rev. Lett.* **92**, 187002 (2004).
3. R. J., H., M., A., H., L. & M., S. in *Proceedings of the International Symposium - Superconductivity and Pressure: A Fruitful Relationship on the Road to Room Temperature Superconductivity*. (in Proceedings of the International Symposium - Superconductivity and Pressure: A Fruitful Relationship on the Road to Room Temperature Superconductivity(ed. Alario-Franco, M. A.) 199–213 (Fundación Ramón Areces, 2019).).
4. Mao, H. & Hemley, R. J. Ultrahigh-pressure transitions in solid hydrogen. *Rev. Mod. Phys.* **66**, 671–692 (1994).
5. Gregoryanz, E. *et al.* Everything you always wanted to know about metallic hydrogen but were afraid to ask. *Matter and Radiation at Extremes* **5**, 038101 (2020).
6. Bi, T., Zarifi, N., Terpstra, T. & Zurek, E. The Search for Superconductivity in High Pressure Hydrides. in *Reference Module in Chemistry, Molecular Sciences and Chemical Engineering* (Elsevier, 2019).
7. Zurek, E. & Bi, T. High-temperature superconductivity in alkaline and rare earth polyhydrides at high pressure: A theoretical perspective. *J. Chem. Phys.* **150**, 050901 (2019).
8. Errea, I. *et al.* Quantum hydrogen-bond symmetrization in the superconducting hydrogen sulfide system. *Nature* **532**, 81–84 (2016).
9. Snider, E. *et al.* Room-temperature superconductivity in a carbonaceous sulfur hydride. *Nature* **586**, 373–377 (2020).
10. Miao, M., Sun, Y., Zurek, E. & Lin, H. Chemistry under high pressure. *Nature Reviews Chemistry* **4**, 508–527 (2020).
11. Peng, F. *et al.* Hydrogen Clathrate Structures in Rare Earth Hydrides at High Pressures: Possible Route to Room-Temperature Superconductivity. *Phys. Rev. Lett.* **119**, 107001 (2017).

12. Liang, X. *et al.* Potential high-Tc superconductivity in CaYH₁₂ under pressure. *Phys. Rev. B* **99**, 100505 (2019).
13. Li, X. *et al.* Polyhydride CeH₉ with an atomic-like hydrogen clathrate structure. *Nature Communications* **10**, 3461 (2019).
14. Wang, H., Tse, J. S., Tanaka, K., Iitaka, T. & Ma, Y. Superconductive sodalite-like clathrate calcium hydride at high pressures. *PNAS* **109**, 6463–6466 (2012).
15. Ye, X., Zarifi, N., Zurek, E., Hoffmann, R. & Ashcroft, N. W. High Hydrides of Scandium under Pressure: Potential Superconductors. *J. Phys. Chem. C* **122**, 6298–6309 (2018).
16. Semenok, D. V. *et al.* Superconductivity at 161 K in thorium hydride ThH₁₀: Synthesis and properties. *Materials Today* **33**, 36–44 (2020).
17. Kruglov, I. A. *et al.* Uranium polyhydrides at moderate pressures: Prediction, synthesis, and expected superconductivity. *Science Advances* **4**, eaat9776 (2018).
18. Zhou, D. *et al.* Superconducting praseodymium superhydrides. *Science Advances* **6**, eaax6849 (2020).
19. Flores-Livas, J. A., Sanna, A. & Gross, E. K. U. High temperature superconductivity in sulfur and selenium hydrides at high pressure. *Eur. Phys. J. B* **89**, 63 (2016).
20. Pickard, C. J., Errea, I. & Eremets, M. I. Superconducting Hydrides Under Pressure. *Annu. Rev. Condens. Matter Phys.* **11**, 57–76 (2020).
21. Errea, I. *et al.* Quantum crystal structure in the 250-kelvin superconducting lanthanum hydride. *Nature* **578**, 66–69 (2020).
22. Azadi, S., Monserrat, B., Foulkes, W. M. C. & Needs, R. J. Dissociation of High-Pressure Solid Molecular Hydrogen: A Quantum Monte Carlo and Anharmonic Vibrational Study. *Phys. Rev. Lett.* **112**, 165501 (2014).
23. McMahon, J. M. & Ceperley, D. M. Ground-State Structures of Atomic Metallic Hydrogen. *Phys. Rev. Lett.* **106**, 165302 (2011).
24. Goncharov, A. Phase diagram of hydrogen at extreme pressures and temperatures; updated through 2019 (Review article). *Low Temperature Physics* **46**, 97–103 (2020).
25. Howie, R. T., Guillaume, C. L., Scheler, T., Goncharov, A. F. & Gregoryanz, E. Mixed Molecular and Atomic Phase of Dense Hydrogen. *Phys. Rev. Lett.* **108**, 125501 (2012).
26. Dronskowski, R. & Bloechl, P. E. Crystal orbital Hamilton populations (COHP): energy-resolved visualization of chemical bonding in solids based on density-functional calculations. *J. Phys. Chem.* **97**, 8617–8624 (1993).
27. Silvi, B. & Savin, A. Classification of chemical bonds based on topological analysis of electron localization functions. *Nature* **371**, 683–686 (1994).
28. Chen, W. *et al.* Synthesis of molecular metallic barium superhydride: pseudocubic BaH₁₂. *Nature Communications* **12**, 273 (2021).
29. Miao, M.-S. & Hoffmann, R. High Pressure Electrides: A Predictive Chemical and Physical Theory. *Acc. Chem. Res.* **47**, 1311–1317 (2014).
30. Miao, M. & Hoffmann, R. High-Pressure Electrides: The Chemical Nature of Interstitial Quasiatoms. *J. Am. Chem. Soc.* **137**, 3631–3637 (2015).
31. Naumov, I. I. & Hemley, R. J. Aromaticity, Closed-Shell Effects, and Metallization of Hydrogen. *Acc. Chem. Res.* **47**, 3551–3559 (2014).
32. Carey, F. A. & Sundberg, R. J. *Advanced Organic Chemistry, Part A: Structure and Mechanisms*. (Springer, 2008).
33. Pauling, L. *The Nature of the Chemical Bond*. (Cornell University Press, 1960).
34. Liu, L. *et al.* Microscopic mechanism of room-temperature superconductivity in compressed LaH₁₀. *Phys. Rev. B* **99**, 140501 (2019).

35. Salke, N. P. *et al.* Synthesis of clathrate cerium superhydride CeH₉ at 80-100 GPa with atomic hydrogen sublattice. *Nature Communications* **10**, 4453 (2019).
36. Semenok, D. V., Kvashnin, A. G., Kruglov, I. A. & Oganov, A. R. Actinium Hydrides AcH₁₀, AcH₁₂, and AcH₁₆ as High-Temperature Conventional Superconductors. *J. Phys. Chem. Lett.* **9**, 1920–1926 (2018).
37. Hooper, J., Altintas, B., Shamp, A. & Zurek, E. Polyhydrides of the Alkaline Earth Metals: A Look at the Extremes under Pressure. *J. Phys. Chem. C* **117**, 2982–2992 (2013).
38. Sun, Y., Lv, J., Xie, Y., Liu, H. & Ma, Y. Route to a Superconducting Phase above Room Temperature in Electron-Doped Hydride Compounds under High Pressure. *Phys. Rev. Lett.* **123**, 097001 (2019).
39. Wei, Y. K. *et al.* Formation and superconducting properties of predicted ternary hydride ScYH₆ under pressures. *International Journal of Quantum Chemistry* **121**, e26459 (2021).
40. Muramatsu, T. *et al.* Metallization and Superconductivity in the Hydrogen-Rich Ionic Salt BaReH₉. *J. Phys. Chem. C* **119**, 18007–18013 (2015).
41. Shi, L.-T. *et al.* Prediction of pressure-induced superconductivity in the novel ternary system ScCaH_{2n} (n = 1–6). *J. Mater. Chem. C* **9**, 7284–7291 (2021).
42. Hutcheon, M. J., Shipley, A. M. & Needs, R. J. Predicting novel superconducting hydrides using machine learning approaches. *Phys. Rev. B* **101**, 144505 (2020).
43. Kresse, G. & Furthmüller, J. Efficiency of ab-initio total energy calculations for metals and semiconductors using a plane-wave basis set. *Comput. Mater. Sci.* **6**, 15–50 (1996).
44. Kresse, G. & Furthmüller, J. Efficient iterative schemes for ab initio total-energy calculations using a plane-wave basis set. *Phys. Rev. B* **54**, 11169–11186 (1996).
45. Kresse, G. & Joubert, D. From ultrasoft pseudopotentials to the projector augmented-wave method. *Phys. Rev. B* **59**, 1758–1775 (1999).
46. Blöchl, P. E. Projector augmented-wave method. *Phys. Rev. B* **50**, 17953–17979 (1994).
47. Perdew, J. P., Burke, K. & Ernzerhof, M. Generalized gradient approximation made simple. *Phys. Rev. Lett.* **77**, 3865–3868 (1996).
48. Zhao, X.-G. *et al.* JAMIP: an artificial-intelligence aided data-driven infrastructure for computational materials informatics. *Science Bulletin* (2021) doi:10.1016/j.scib.2021.06.011.
49. Bader, R. F. W. *Atoms in Molecules: A Quantum Theory*. (Clarendon Press, 1994).
50. Frisch, M. J. *et al.* *Gaussian 16 Rev. C.01*. (2016).
51. Becke, A. D. Density-functional thermochemistry. III. The role of exact exchange. *J. Chem. Phys.* **98**, 5648–5652 (1993).
52. Lee, C., Yang, W. & Parr, R. G. Development of the Colle-Salvetti correlation-energy formula into a functional of the electron density. *Phys. Rev. B* **37**, 785 (1988).
53. Miehlich, B., Savin, A., Stoll, H. & Preuss, H. Results obtained with the correlation energy density functionals of becke and Lee, Yang and Parr. *Chemical Physics Letters* **157**, 200–206 (1989).
54. Tsuchimochi, T. & Scuseria, G. E. Communication: ROHF theory made simple. *J. Chem. Phys.* **133**, 141102 (2010).

Acknowledgements: M.M. and Y.S. acknowledge the support of NSF CAREER award 1848141, M.M. also acknowledges the support of ACS PRF 59249-UNI6 and the support of California State University Research, Scholarship and Creative Activity (RSCA) award. We thank the computational resources provided by XSEDE (TG-DMR130005).

Author contributions: M.M. proposed the chemical template mechanism and designed the research. Y.S. conducted all the calculations. M.M. and Y.S. analyzed the results together. M.M. wrote the manuscript. M.M. and Y.S. plotted the figures together.

Competing interests: The authors declare no competing interests.

Supplementary Information

Chemical templates that assemble the metal superhydrides

Yuanhui Sun and Maosheng Miao*

Department of Chemistry and Biochemistry, California State University Northridge, CA USA

*Email: mmiao@csun.edu

Supplementary Material

Section I. Energetics of H incorporated in superhydrides	23
Section II. The building units of H lattices and their aromaticity.....	25
Section III. The chemical templates in various superhydrides	30
Section IV. The normal stresses of the metal sub-lattices in superhydrides.....	35
Section V. The chemical templates strengths in MH_6 , MH_{10} and MH_9	36
Section VI. Stabilization of H units in superhydrides lattice.....	38
Section VII. Charge transfers in views of chemical bonds and chemical templates	39
Section VIII. The chemical templates and stability of mixed metal superhydrides	40
References.....	43

Section I. Energetics of H incorporated in superhydrides

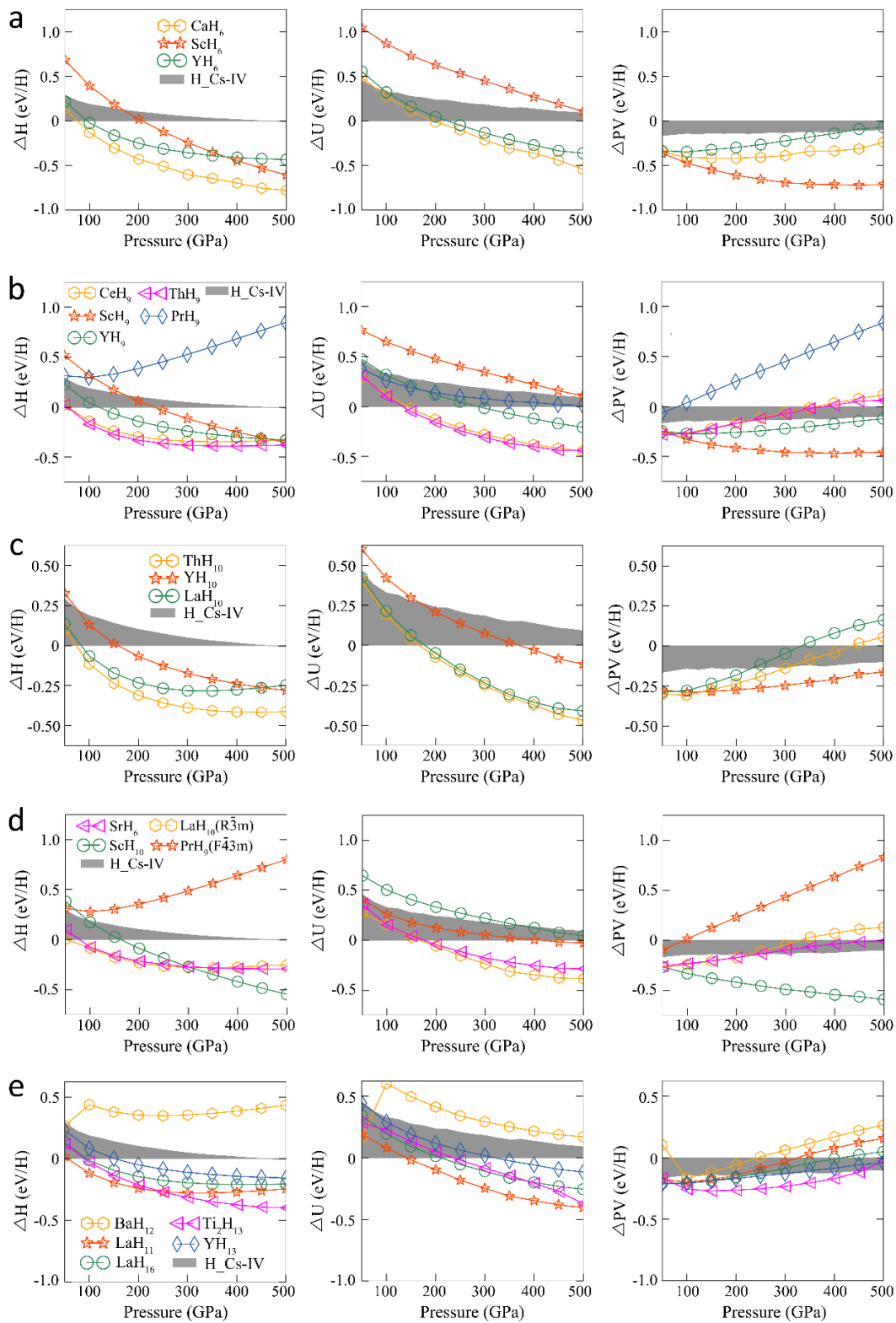


Fig. 1: The extracted enthalpy (ΔH), internal energy (ΔU) and $P\Delta V$ term of hydrogen in superhydrides relative to pristine hydrogen in molecular phase as functions of pressure. The investigated superhydrides include: **a**, CaH_6 , ScH_6 , YH_6 in $Im\bar{3}m$ structure; **b**, CeH_9 , ScH_9 , YH_9 , ThH_9 , PrH_9 in $P6_3/mmc$ structure; **c**, ThH_{10} , YH_{10} , LaH_{10} in $Fm\bar{3}m$ structure; **d**, SrH_6 in $R\bar{3}m$ structure, ScH_{10} in $P6_3/mmc$ structure, PrH_9 in $F\bar{4}3m$ structure, LaH_{10} in $R\bar{3}m$ structure, and **e**, BaH_{12} in $Fm\bar{3}m$ structure, LaH_{11} in $P4nmm$ structure, LaH_{16} in $P6/mmm$ structure, Ti_2H_{13} in $Immm$ structure, YH_{13} in $R\bar{3}m$ structure. All quantities are relative to that of molecular H C_2/c structure. The shaded areas show ΔH , ΔU , and $P\Delta V$ of metallic H in Cs-IV structure.

Section II. The building units of H lattices and their aromaticity

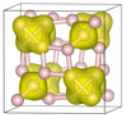
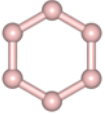
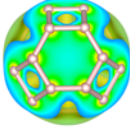
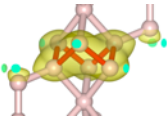
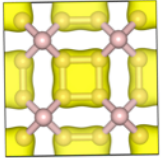
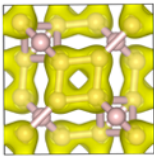
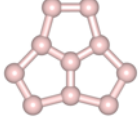
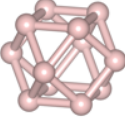
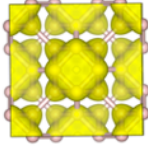
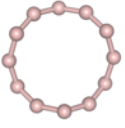
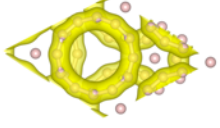
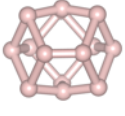
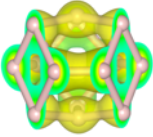
Name	Compounds	Structure	Wavefunction	Energy Levels
H ₄ tetrahedron	MH ₉ M=Pr ^{1,2} , Pa ³			— $\uparrow\downarrow$ -4.61 — -3.12 $\uparrow\downarrow$ -14.51
H ₆ hexagon	MH ₆ M=Ca ⁴ , Sc ⁵⁻⁷ , Y ^{8,9}			— — 5.21 — -0.79 $\uparrow\downarrow$ $\uparrow\downarrow$ -13.65 $\uparrow\downarrow$ -9.69
H ₆ corona	MH ₉ M = Sc ¹ , Y ¹ , Th ¹⁰ , Ce ^{11,12} , Pr ² , U ¹³			— — -1.06 — 1.53 $\uparrow\downarrow$ $\uparrow\downarrow$ -16.81 $\uparrow\downarrow$ -8.82
H ₈ cube	MH ₁₀ M=La ^{1,14-17} , Y ¹ , Th ^{10,18}			— — 8.02 — 0.14 $\uparrow\downarrow$ $\uparrow\downarrow$ -19.80 $\uparrow\downarrow$ -10.01
H ₈ deformed cube	MH ₉ M=Pr ^{1,2} , Pa ³			— — 5.71 — 0.28 $\uparrow\downarrow$ $\uparrow\downarrow$ -9.95 $\uparrow\downarrow$ -20.11
H ₁₀ Tripentagon	MH ₁₀ M= Sc ¹⁹ , Zr ¹⁹ , Hf ¹⁹ , Lu ¹⁹			-6.13 $\uparrow\downarrow$ -5.10 $\uparrow\downarrow$ -6.92 $\uparrow\downarrow$ $\uparrow\downarrow$ -13.57 $\uparrow\downarrow$ -20.29
H ₁₂ Cuboctahedron	MH ₁₂ M= Ba ²⁰			2.40 — — 2.01 $\uparrow\downarrow$ — -2.14 $\uparrow\downarrow$ -7.73 $\uparrow\downarrow$ $\uparrow\downarrow$ -17.13 $\uparrow\downarrow$ -17.52 $\uparrow\downarrow$ -25.97
H ₁₂ Ring	MH ₁₃ M=Y ¹			— — 2.20 -4.17 — $\uparrow\downarrow$ -5.02 $\uparrow\downarrow$ $\uparrow\downarrow$ -15.42 $\uparrow\downarrow$ -10.39 $\uparrow\downarrow$ -14.04
H ₁₄ Cage	MH ₁₆ M = La ²¹			-1.58 — — -1.59 $\uparrow\downarrow$ $\uparrow\downarrow$ -10.50 $\uparrow\downarrow$ -8.55 $\uparrow\downarrow$ $\uparrow\downarrow$ -19.27 $\uparrow\downarrow$ -18.04 $\uparrow\downarrow$ -26.16

Table 1. The structures and the energy levels of H clusters (building units) in superhydrides. They are identified by geometries and wavefunctions of the H lattice after removing all metal atoms in superhydrides.

Another important structure feature of the superhydrides is that their H lattices consist of building units that show unique electronic structure features, including being aromatic. Aromaticity is a concept for organic molecules consisting of conjugated π bonds formed by the p orbitals of consisting atoms. The corresponding molecular orbitals are delocalized because each p orbital can bond resonantly with two or more neighboring p orbitals. The most common examples are those formed by C 2p orbitals. Because of the topological nature of the 2p orbitals, the C atoms need to locate in the same plane in aromatic molecules or groups. The essence of the aromaticity is that the energy levels of the π orbitals form a gap, below which all the levels are occupied and above which all the level are empty. Because of the coplanar constraint, the π orbitals come in pairs except the lowest energy one that corresponds to the overall bonding state and does not contain any node. Therefore, the π systems containing $4n+2$ electrons are aromatic because they fill the $2n+1$ orbitals and form a gap. The size of the gap corresponds to the strength of the aromaticity, and the larger the gap, the stronger the aromaticity. In contrast to π bonds, the σ bonds are usually formed by sp^n ($n=3,2,1$) hybrid orbitals. These bonds are localized in the region between the two bonding atoms because, each hybrid orbital can only form bond with another orbital in one direction (head to head). On the other hand, the sp^3 hybridized orbitals can form three-dimensional covalent networks, which becomes the structural framework for organic molecules and many covalent crystals.

The H-H bonds in superhydrides as well as in atomic hydrogen share the features of both the π bonds of p orbitals and σ bonds of hybrid orbitals. These bonds are formed by the 1s orbitals of two neighboring H atoms. Similar to σ bonds, they can form 3D networks as in superhydrides or in atomic hydrogen phases. On the other hand, one 1s orbital can form multiple bonds with neighboring H atoms resonantly in a similar way as the π bonds in organic molecules. However, because the 1s orbital is spherical, the conjugation of the 1s-1s bonds does not require these bonds to be coplanar. This major difference between the H-H bonds and the C-C π bonds lifts the coplanar constraint of aromaticity. Thus, a 3D H cluster could still be aromatic, if the occupation of its energy levels satisfies the requirement of aromaticity, i.e. the lower energy orbitals are fully occupied and the higher energy orbitals are empty, forming a gap between the HOMO and the LUMO orbitals. Eventually, the aromaticity depends on the symmetry and the number of electrons of the cluster. Strikingly, we find that the H lattices of most of the superhydrides consist of building units that are aromatic. Especially, these units locate at the high value regions of ELF, often corresponding to maxima, and

therefore are largely stabilized by the electrons localized in these regions. The following summarizes the most important building units found in the superhydrides that have been discovered so far.

H₄ tetrahedrons are found in $F\bar{4}3m$ MH₉ (M=Pr etc.) compounds. The four electrons fill the two lower energy orbitals and the two degenerate levels with higher energy are empty. It has a gap of 1.49 eV if the geometry parameters are taken from PrH₉ at 400 GPa. In MH₉ superhydrides, the H₄ tetrahedrons locate at the tetrahedral interstitial sites where the ELF shows maxima.

H₆ hexagons are found in $Im\bar{3}m$ MH₆ superhydrides. Many metals such as Ca, Sc, Y and La etc. can form these superhydrides. The deformed H₆ hexagons, such as elongated H₆, can be found in several other types of superhydrides, such as $Fm\bar{3}m$ MH₁₀ and $Immm$ M₂H₁₃ etc. The H₆ hexagon is analogous to benzene molecules. Its aromaticity has been thoroughly discussed previously and has been used to explain the stability of atomic hydrogen phases that consist of “graphene-like” hydrogen layered structures. The H-H distance in H₆ hexagons in LaH₆ at 300 GPa is 1.234 Å, and the corresponding HOMO-LUMO gap is found to be 8.50 eV, indicating a strong aromaticity.

H₆ corona is found in $P6_3/mmc$ MH₉ superhydrides. All 6 H atoms are equivalent. The H-H distance is 1.118 Å for CeH₉ at 300 GPa. It is also aromatic and has a large gap of 8.76 eV, similar to H₆ hexagon. Interestingly, the LUMO of H₆ corona is a single orbital, which is different to the doubly degenerate LUMO in H₆ hexagons. In MH₉ compounds, H₆ coronas locate at the octahedral interstitial sites and are significantly stabilized by the high distribution of electrons.

H₈ cube is found in $Fm\bar{3}m$ MH₁₀ superhydrides. The well-known example is LaH₁₀. The H-H distances in H₈ cube in LaH₁₀ at 300 GPa are 1.146 Å. This is actually longer than the H¹-H² distances that connect the H₈ cubes and the H² atoms at the tetrahedral sites. The later is 1.064 Å in LaH₁₀ at 300 GPa. Still, the wavefunctions show that H₈ cube is a building unit. H₈ cube show very strong aromaticity with a gap between its HOMO and LUMO states as high as 10.15 eV. Due to the highly symmetric geometry, both HOMO and LUMO orbitals are triply degenerate. In MH₁₀ superhydrides, H₈ cubes locate at the octahedral sites and are largely stabilized by the large electron localizations as revealed by the metal ELF.

Deformed H₈ cube presents in $F\bar{4}3m$ MH₉ superhydrides. It can be obtained by deforming the cube in a way that all faces become slightly bended rhombus. All H atoms are equivalent and there is only one nearest H-H distance. It has a value of 1.149 Å in PrH₉ at 400 GPa. The two angles of the rhombus are 78.04° and 100.80°, and the dihedral angle of the bended rhombus is 11.61°. With these geometry parameters, the energy levels of the deformed H₈ cube are calculated. Despite the lowering of the symmetry, the energy levels are similar to the original H₈ cube. Especially, the HOMO and LUMO orbitals are triply degenerate. It also shows a large gap of 10.23 eV, indicating strong aromaticity. Similar to H₈ cube, the deformed H₈ cubes also locate at the octahedral sites of FCC metal lattice and are greatly stabilized by the high electron distributions in these regions.

H₁₀ tripentagons are found in $P6_3/mmc$ MH₁₀ superhydrides. DFT calculations predicted the formation of such compounds for several metals including Sc, Zr, Lu and Hf, etc. While concerning the H lattices, this type of superhydrides is quite unique. First, the H atoms do not form an extended covalent network. Instead, they form planar H₁₀ molecules. The structure of these molecules is analogous to acepentalene (C₁₀H₆) and consists of three pentagons connected by sharing edges. There are three H-H distances. For ScH₁₀ at 300 GPa, the H-H distance between the center H and its three neighbors (H that are shared by two neighboring pentagons) is 0.915 Å, the H-H distance between the shared H and its neighboring edge H is 1.067 Å, and the H-H distance between two edge H atoms is 1.007 Å. The Gaussian calculation of the electronic structure of H₁₀ molecule with the same geometry as H₁₀ in ScH₁₀ at 300 GPa shows a small gap of 1.03 eV between its non-degenerate HOMO and LUMO levels.

H₁₂ cuboctahedrons exist in $Fm\bar{3}m$ MH₁₂ superhydrides. Comparing with cubic MH₁₀ structure, all H atoms locate at octahedral interstitials and form cuboctahedrons. In BaH₁₂ at 135 GPa, the shortest H-H distance within H₁₂ is 1.271 Å, whereas the shortest H-H distance between the neighboring H₁₂ is 1.344 Å. All H atoms are equivalent in cuboctahedrons. With the above geometry, the energy levels are calculated using Gaussian program. The HOMO levels are doubly degenerate whereas the LUMO is not. The gap between the HOMO and the LUMO levels is found to be 5.59 eV, showing moderate aromaticity. Like all other H clusters, the H₁₂ cuboctahedrons are also stabilized by the electron distributions at the octahedral sites in metal FCC lattices.

H₁₂ ring is a striking unit found in $R\bar{3}m$ MH₁₃ compounds. Its large size (3.900 Å diameter in YH₁₃ at 200 GPa) and unusual shape make it difficult for close packing under high pressure. However, both the geometry and the wavefunctions distinctly reveal their existence. For YH₁₃ at 200 GPa, the H-H bond length within the ring is 1.025 Å, whereas the shortest H-H distance between the rings is 1.224 Å and the shortest distance between H on the ring and the H between the layers is 1.210 Å. Different to other H units, H₁₂ ring is an analogue to C π bonds, therefore should also follow the Hückel 4n+2 rule. Based on this rule, H₁₂ ring is anti-aromatic, i.e. the doubly degenerate HOMO levels are half filled. However, in the YH₁₃ structure, the H₁₂ ring is slightly distorted. Among 12 H atoms, 6 remain in the original position, 3 move upwards and 3 downwards alternatively, creating a wave-like modulation. As the result of this deformation, a gap of 0.85 eV is opened. As discussed in the previous section, H₁₂ ring matches the ELF high value regions of the metal lattice and therefore its stability is enhanced by the template effect.

H₁₄ cage can be viewed as the structure unit of the H lattice in P6/mmm MH₁₆ superhydrides. Not all the H atoms are equivalent and there are three different H-H distances in the cage. The H-H distance of the top H to its three neighbors (second layer) is 1.074 Å, and the H-H distance that connects the second and the third layer H atoms is 1.271 Å. Lastly, the two neighboring H atoms in the third layer has a distance of 1.011 Å. The unit is aromatic and shows a gap of 6.96 eV between its doubly degenerate HOMO levels and the single LUMO level. In MH₁₆ structures, the H₁₄ cages are connected by sharing the H₄ rings at its three sides, and form a 2D layered structure with hexagonal symmetry. The 2D hexagonal lattice matches well with the ELF of the metal lattice and are stabilized by the electrons localized in the region.

Section III. The chemical templates in various superhydrides

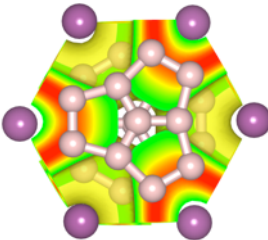
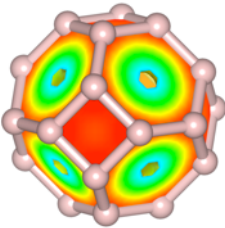
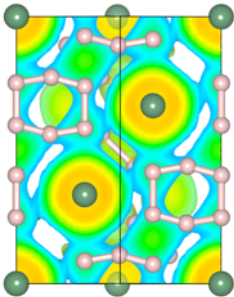
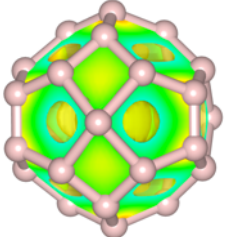
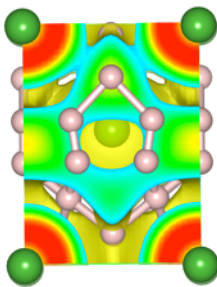
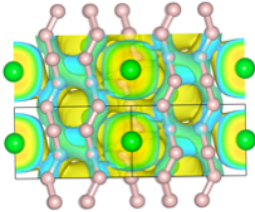
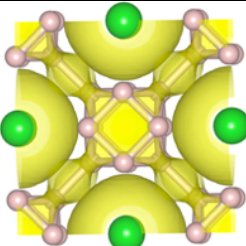
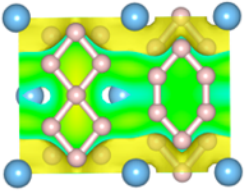
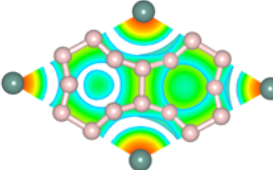
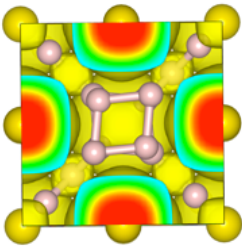
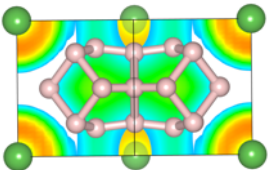
Compound (symmetry)	Metal Lattice	Metal ELF overlay on H lattice	MH ₁₀ (<i>P6₃/mmc</i>)	HCP M= Sc ¹⁹ , Zr ¹⁹ , Hf ¹⁹ , Lu ¹⁹	
MH ₆ (<i>Im</i> $\bar{3}$ <i>m</i>)	BCC M=Ca ⁴ , Sc ⁵⁻⁷ , Y ^{8,9}		MH ₁₀ (<i>R</i> $\bar{3}$ <i>m</i>)	Hex** M = Ac ²⁵	
MH ₉ (<i>P6₃/mmc</i>)	HCP M = Sc ¹ , Y ¹ , Th ¹⁰ , Ce ^{11,12} , Pr ² , U ¹³		MH ₁₁ (<i>P4nmm</i>)	BCT M = La ^{1,21}	
MH ₆ (<i>R</i> $\bar{3}$ <i>m</i>)	dBCC* M = Sr ^{22,23}		MH ₁₂ (<i>Fm</i> $\bar{3}$ <i>m</i>)	FCC M = Ba ²⁰	
M ₂ H ₁₃ (<i>Immm</i>)	M=Ti ²⁴		MH ₁₃ (<i>R</i> $\bar{3}$ <i>m</i>)	FCC R- 3m M=Y ¹	
MH ₉ (<i>F</i> $\bar{4}$ <i>3m</i>)	FCC M=Pr ^{1,2} , Pa ³		MH ₁₆ (<i>P6/mmm</i>)	SH M = La ²¹	

Table 2. The ELF's are calculated for metal lattices in superhydrides. The results are overlaid on H lattice. The small white balls represent H atoms, and the metal atoms, if visible, are represented by colored balls. *dBCC is distorted BCC. **Hex is an FCC deformed along (111).

$Fm\bar{3}m$ LaH₁₀. The chemical template mechanism is based on a striking feature of superhydrides that are emerged from electronic structure calculations. It can be revealed by calculating the ELF of the metal lattices in superhydrides after removing all H atoms. For example, the La atoms form an FCC lattice in LaH₁₀ superhydrides. For LaH₁₀ at 300 GPa, the La lattice corresponds to an FCC La at 12.4 GPa. The ELF of this metal structure is calculated and found to have large values and maxima at octahedral and tetrahedral interstitial sites. ELF is known to reveal the chemical structure of atoms, molecules and solids. For example, it can clearly reveal the shell structure and the orbitals of heavy atoms whereas the electron density decreases monotonically with increasing radial distance. Thus, the ELF maxima at the interstitial sites of FCC La indicate that some crystal orbitals have large contributions in these regions. In other words, these crystal orbitals consist of large compositions of the local orbitals of the quasi-atoms locating at these interstitial sites. As discussed in the text, we can identify the crystal orbitals that correspond to the occupation of quasi-atom orbitals at the interstitial sites. Since the electrons do not localize completely at these interstitial sites, it is not a high-pressure electride (HPE).

The large electron distributions at the interstitial sites act as an effective chemical template for the assembly of H lattice in LaH₁₀ because they match nicely with the H₁₀ lattice. As shown in Fig. 2a and 4b, the H₈ cubes and the H² atoms of the H lattice in LaH₁₀ locate exactly at the E^O and E^T interstitial sites.

$Im\bar{3}m$ MH₆ (M=Ca, Sc, Y etc.) The metal atoms form a BCC lattice. The ELF shows large values at the octahedral interstitial sites. Once overlaid on the H₆ lattice, it shows large values on the sites of the H atoms, especially it matches well with the H₄ and H₆ rings in the H lattice.

$P6_3/mmc$ MH₉ (M=Ce, Y etc.) The metal atoms form an HCP lattice. The ELF has maxima at the octahedral and tetrahedral interstitial sites. Again, it matches well with the H lattice in MH₉ superhydrides as shown in Fig. 4c and Supplementary Table 2. The H₆ corona locates at the octahedral sites whereas the two center H atoms in H₈ bipyramid units locate close to the neighboring tetrahedral sites.

$R\bar{3}m$ MH₆ (M=Sr) The metal atoms form a deformed BCC lattice ($R\bar{3}m$). It can be viewed as compressing an BCC lattice along the (111) diagonal direction. The ELF shows maxima at metal sites as well as the interstitial sites. With

an isosurface value of 0.3, the ELF surface forms a 3D structure consisting of connected wavy chains along the perpendicular direction. Strikingly, this connected chain structure matches very well the H lattice in SrH₆, which consists of zigzag H chains. The H-H distances in the chain is 1.015 Å at 250 GPa, whereas the shortest H-H distances between the neighboring chains is 1.411 Å.

***Immm* M₂H₁₃ (M=Ti)** This superhydride is found to adopt a layered structure. In each layer, the H atoms form two ribbons. One ribbon consists of a chain of double-rhombus; and the other consists of isolated elongated hexagons. The H-H distances in these elongated hexagons are 1.023 and 1.048 Å. The H-H distances between two hexagons are 1.815 Å, ruling out the connection by a covalent bond. In contrast, the H-H distance between the double-rhombus is only 0.865 Å, indicating the presence of H₂ molecules. This ribbon can also be viewed as connected H₂ molecules and square planar H₅ units. Despite the complicated structure of H lattice, it matches very well the ELF maxima of the metal lattice. As shown in Supplementary Table 2, the ELF also show layered feature. Especially, it shows large values in the regions where the double-rhombus and the elongated H₆ hexagons locate. Interestingly, the locations of the H₂ molecules correspond to regions of minimum ELF.

***F $\bar{4}3m$* MH₉ (M=Pr)** The structures can be viewed as a deformed LaH₁₀ structure. Although the symmetry is lower than that of MH₁₀, the metal lattice maintains an FCC structure. Therefore, its ELF is the same as in MH₁₀, and show maxima at both the octahedral and the tetrahedral interstitial sites. There are two major differences between the H₉ lattice in this compound and the H₁₀ lattice in MH₁₀. First, half of the H² atoms are replaced by H₄ tetrahedrons at the tetrahedral sites. Second, the H₈ cubes are deformed to match the lower symmetry caused by the replacement of H² atoms by H₄ tetrahedrons. Nevertheless, the H₉ lattice matches well with the ELF, with deformed H₈ cubes locating at the octahedral sites and the H² atoms and H₄ tetrahedrons occupying the tetrahedral sites.

***P6₃/mmc* MH₁₀ (M=Sc, Zr, Lu, Hf etc.)** Different to other MH₁₀ superhydrides, these compounds adopt a hexagonal layered structure (*P6₃/mmc*). Each layer contains 1 metal atom and 10 H atoms positions in a hexagonal lattice. Another important feature is that the H in these compounds do not form extended covalent network. Instead, they form H₁₀ planar molecules with the same geometry of acepentalene (C₁₀H₆). The metal lattice is an HCP reduced in perpendicular direction. The ELF of this metal lattice shows rings of large value maxima locating at the B sites (if

the metals locate at A sites). The highest values at the interstitial regions are as large as 0.65 for Sc. The H₁₀ molecule locate in between the ELF rings, with three of its edges (2 H atoms) locating in the high ELF value region, and the H atoms sharing two pentagons locating in the medium ELF value regions. The center H atoms locate at ELF minima.

$R\bar{3}m$ MH₁₀ (M=Ac etc.) The metal lattice of this superhydride is very close to an FCC lattice. It is slightly compressed along the (111) diagonal direction. The M-M distances inside the [111] layer are 3.688 Å whereas the M-M distances between neighboring layers are 3.497 Å. Nevertheless, the H lattice is very different to cubic MH₁₀. It is a semi-layered structure. The in-layer H-H distances are 1.085 and 1.099 Å, whereas the shortest H-H distances between layers are 1.313 Å. Despite the complex structure of H lattice, it matches well with the ELF. Similar to the ELF of an FCC structure, the ELF results of the metals in these compounds also show maxima in the octahedral and the tetrahedral interstitial sites. A deformed H₈ cube locates at each octahedral site, and one H atom occupies each tetrahedral site.

$P4nmm$ MH₁₁ (M=La etc.) The metal atoms form a body-centered tetragonal (BCT) lattice. The lattice parameters at 100 GPa are a=b=3.873 Å and c=5.272 Å. The major interstitial sites are octahedral and locate at the base center. ELF of BCT La shows maxima at these sites. The H lattice matches fairly well with the ELF distribution.

$Fm\bar{3}m$ MH₁₂ (M=Ba etc.) This type of superhydrides has the same symmetry group ($Fm\bar{3}m$) as cubic LaH₁₀. Therefore, its metal atoms form an FCC lattice. The ELF shows maxima at both the octahedral and interstitial sites. The major difference is the H lattice. The H lattice in MH₁₂ consists of H₁₂ cuboctahedrons (polyhedrons with 12 vertices). They all locate at the octahedral sites of the metal FCC lattice. There is no H atom locating at the tetrahedral sites.

$R\bar{3}m$ MH₁₃ (M=Y etc.) Similar to all other $R\bar{3}m$ superhydrides (MH₆ and MH₁₀), the metal atoms form a deformed FCC by compressing the lattice along (111) diagonal direction. The H lattice shows a very unusual structural feature. Among the 13 H atoms, 12 of them locate in the same layer with the metal atom, forming a large ring circling the metal atom. The H-H distances in the ring are 1.025 Å for YH₁₃ under 200 GPa, the shortest H-H distance between rings is 1.224 Å. One extra H locates between the two layers and at the center site among three H₁₂ rings, and connects

them with a H-H distance of 1.210 Å. The high value regions of ELF match the H lattice including the H₁₂ rings in the layers and the H atoms connecting the rings.

***P6/mmm* MH₁₆ (M=La)** The metal atoms in this superhydrides form a simple hexagonal (SH) lattice. The lattice parameters for both MH₁₆ at 150 GPa and the corresponding SH lattice are a=b=3.692 Å and c=3.707 Å. The H lattice consists of layers. Each layer is formed by connecting H₁₄ cages by their 3 H₄ rhombus sides. There are three H-H distances inside each H₁₄ cage that are 1.074, 1.011 and 1.271 Å. The minimum H-H distance between two neighboring layers is 1.525 Å. The ELF of the metal lattice show maxima at the two interstitial sites centered at the B and C sites of hexagonal lattice (assuming the metal atoms locate at the A sites) and at the center of the two metal layers. It matches very nicely with the H lattice. Each H₁₄ cage centers at an interstitial site.

Section IV. The normal stresses of the metal sub-lattices in superhydrides

	Com- pounds	Press- ure (GPa)	Metal Lattice Pressure (GPa)				Com- pounds	Press- ure (GPa)	Metal Lattice Pressure (GPa)		
MH ₆ (<i>Im</i> $\bar{3}m$)	CaH ₆	300	56.2	56.2	56.2	MH ₁₀ (<i>P</i> 6 ₃ / <i>mmc</i>)	ScH ₁₀	300	9.3	9.3	30.7
	ScH ₆	300	37.0	37.0	37.0		ZrH ₁₀	300	6.5	6.5	26.7
	YH ₆	300	45.8	45.8	45.8		LuH ₁₀	300	13.8	13.8	49.4
					HfH ₁₀		300	5.2	5.2	33.7	
MH ₁₀ (<i>Fm</i> $\bar{3}m$)	LaH ₁₀	300	12.4	12.4	12.4	MH ₁₀ (<i>R</i> $\bar{3}m$)	LaH ₁₀	150	2.1	2.1	4.7
	YH ₁₀	300	16.4	16.4	16.4		AcH ₁₀	200	11.3	11.3	18.7
	ThH ₁₀	300	10.1	10.1	10.1						
MH ₉ (<i>P</i> 6 ₃ / <i>mmc</i>)	ScH ₉	300	11.0	11.0	12.0	MH ₁₁ (<i>P</i> 4 nmm)	LaH ₁₁	100	-1.1	-1.1	-0.6
	YH ₉	300	22.0	22.0	24.1						
	ThH ₉	300	11.9	11.9	35.1						
	CeH ₉	300	1.1	1.1	15.1						
	PrH ₉	300	-3.2	-3.2	8.8						
	UH ₉	300	-17.4	-17.4	-5.0						
MH ₆ (<i>R</i> $\bar{3}m$)	SrH ₆	300	49.2	49.2	59.0	MH ₁₂ (<i>Fm</i> $\bar{3}m$)	BaH ₁₂	135	6.3	6.3	6.3
M ₂ H ₁₃ (<i>I</i> mmm)	Ti ₂ H ₁₃	350	23.1	-6.3	21.5	MH ₁₃ (<i>R</i> $\bar{3}m$)	YH ₁₃	200	4.1	4.1	-7.7
MH ₉ (<i>F</i> $\bar{4}3m$)	PrH ₉	400	4.9	4.9	4.9	MH ₁₆ (<i>P</i> 6/ <i>mmm</i>)	LaH ₁₆	150	-3.5	-3.5	-3.4
	PaH ₉	300	-1.2	-1.2	-1.2						

Table 3. Normal stresses of the metal lattices (after removing all H atoms) in superhydrides under certain pressures.

Section V. The chemical templates strengths in MH_6 , MH_{10} and MH_9

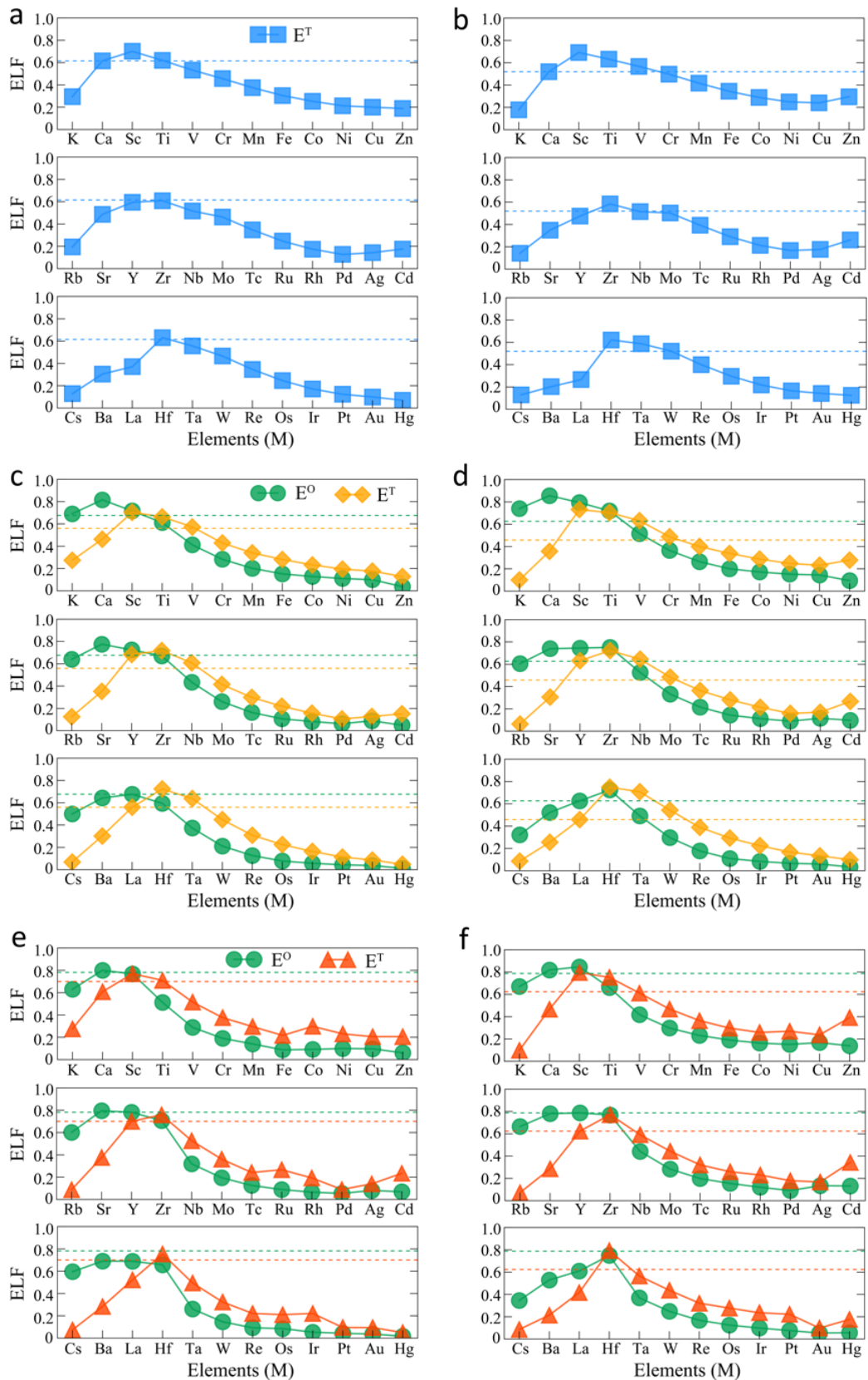


Fig. 2: The ELF values at the interstitial points of metal lattices in MH₆, MH₁₀ and MH₉. **a**, The ELF values at E^T sites of metal BCC lattice with a unit length corresponds to MH₆ superhydrides at 100 GPa. M is a 4th, 5th, and 6th row metal element, respectively. **b**, The ELF values at E^T sites of metal BCC lattice with a unit length corresponds to MH₆ superhydrides at 300 GPa. The blue dashed lines in both **(a)** and **(b)** panels show the ELF values of Ca for comparison. **c**, The ELF values at E^O and E^T sites of metal FCC lattice with a unit length corresponds to MH₁₀ at 100 GPa. M is a 4th, 5th, and 6th row metal element, respectively. **d**, The ELF values at E^O and E^T sites of metal FCC lattice with a unit length corresponds to MH₁₀ at 300 GPa. The green and orange dashed lines show the ELF values of La at E^O and E^T for comparison. **e**, The ELF values at E^O and E^T sites of metal HCP lattice with a unit length corresponds to MH₉ at 100 GPa. M is a 4th, 5th, and 6th row metal element, respectively. **f**, The ELF values at E^O and E^T sites of metal HCP lattice with a unit length corresponds to MH₉ at 100 GPa. The green and red dashed lines show the ELF values of Ce at E^O and E^T for comparison.

Section VI. Stabilization of H units in superhydrides lattice

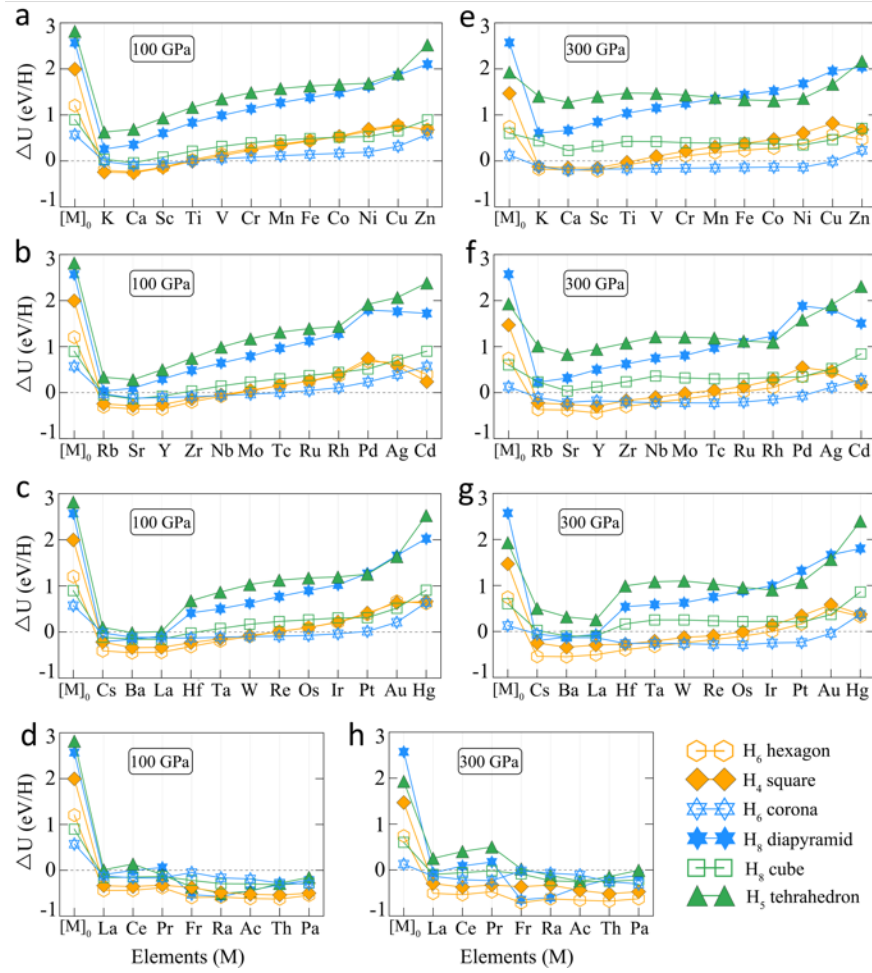


Fig. 3: The change of internal energies while forming H clusters in metal superhydrides. a-d, The energies of the H units relative to H_2 with the presence of metals in the 4th row (panel a), the 5th row (panel b) of periodic table, the 6th row (panel c) of periodic table and several rare earth metals (panel d), calculated by use of the He matrix at 100 GPa (see Methods). $[M]_0$ represents He matrix with no metals. e-h, The energies of the H units relative to H_2 with the presence of metals in the 4th row (panel e), the 5th row (panel f) of periodic table, the 6th row (panel g) of periodic table and several rare earth metals (panel h), calculated by use of the He matrix at 300 GPa.

Section VII. Charge transfers in views of chemical bonds and chemical templates

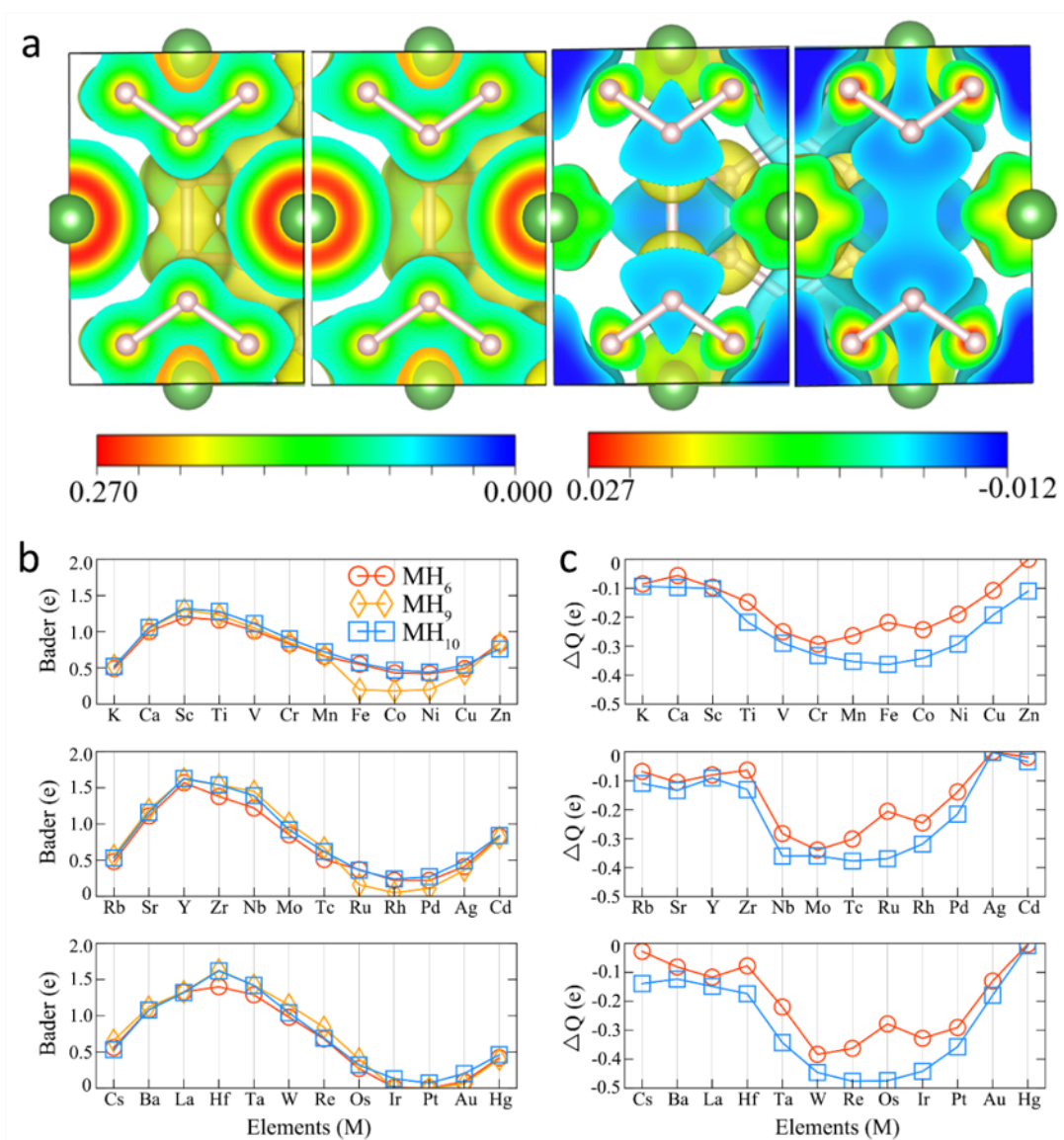


Fig. 4: The charge transfers calculated using free atoms or sub-lattices as the reference states. **a**, From left to right: the charge distribution of LaH_{10} [$\rho(\text{LaH}_{10})$] on (110) plane at 100 GPa; the summation of the charge distributions of La [$\rho(\text{La})$] and H_{10} lattices [$\rho(\text{H}_{10})$] in LaH_{10} compound on (110) plane at 100 GPa; the difference between $\rho(\text{LaH}_{10})$ and $\rho(\text{La}) + \rho(\text{H}_{10})$ at 100 GPa; the difference between $\rho(\text{LaH}_{10})$ and $\rho(\text{La}) + \rho(\text{H}_{10})$ at 300 GPa. **b**, The Bader charges of MH_6 , MH_{10} and MH_9 superhydrides for the 4th, 5th and 6th rows of metal elements. **c**, The integrated differential charge density of metals in MH_6 , MH_{10} and MH_9 superhydrides (see Methods).

Section VIII. The chemical templates and stability of mixed metal superhydrides

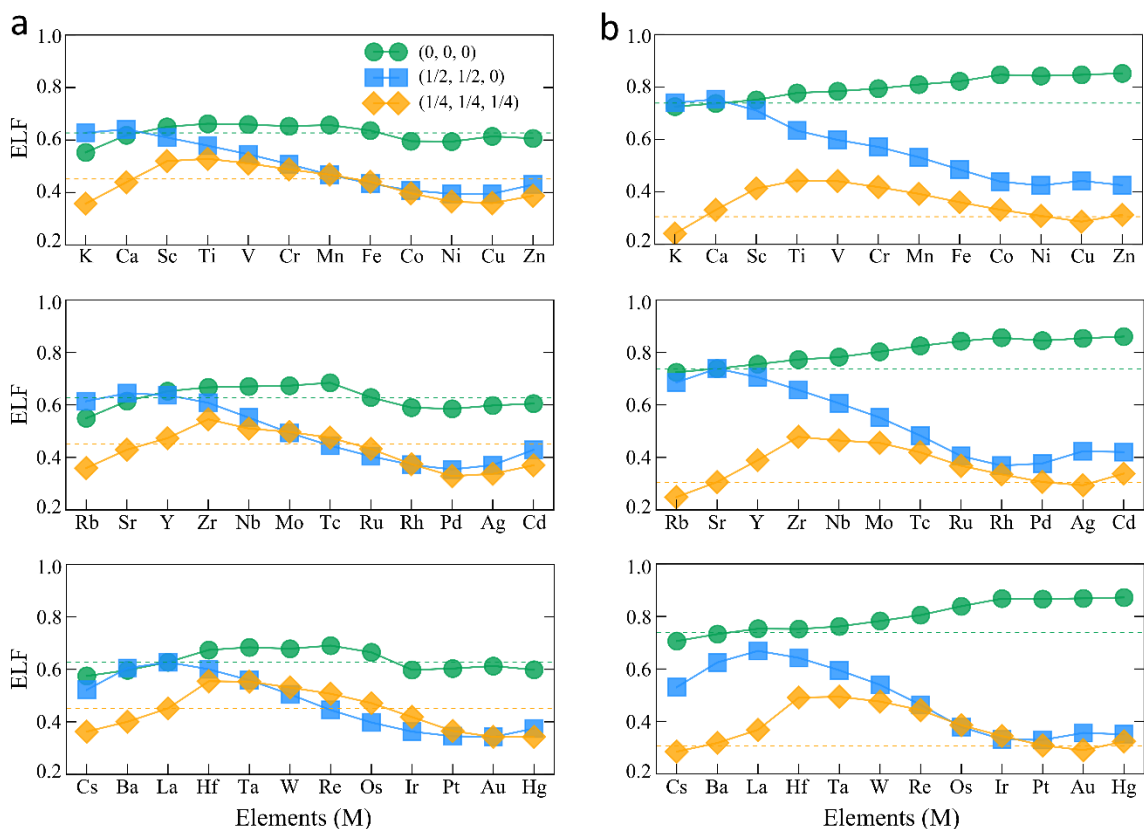


Fig. 5: The change of ELF values while replacing metals in $M\text{H}_{10}$. **a**, The change of ELF values at interstitial sites including (0, 0, 0), (1/2, 1/2, 0) and (1/4, 1/4, 1/4), while replacing one La atom in a conventional cell of LaH_{10} superhydrides at 100 GPa. M is a 4th, 5th, and 6th row metal element, respectively. The green and the orange dashed lines show the ELF values of La FCC at (0,0,0) and (1/4, 1/4, 1/4) points for comparison. **b**, The change of ELF values at interstitial sites including (0, 0, 0), (1/2, 1/2, 0) and (1/4, 1/4, 1/4), while replacing one Sr atom in a conventional cell of SrH_{10} superhydrides at 100 GPa. M is a 4th, 5th, and 6th row metal element, respectively. The green and the orange dashed lines show the ELF values of Sr FCC at (0,0,0) and (1/4, 1/4, 1/4) points for comparison.

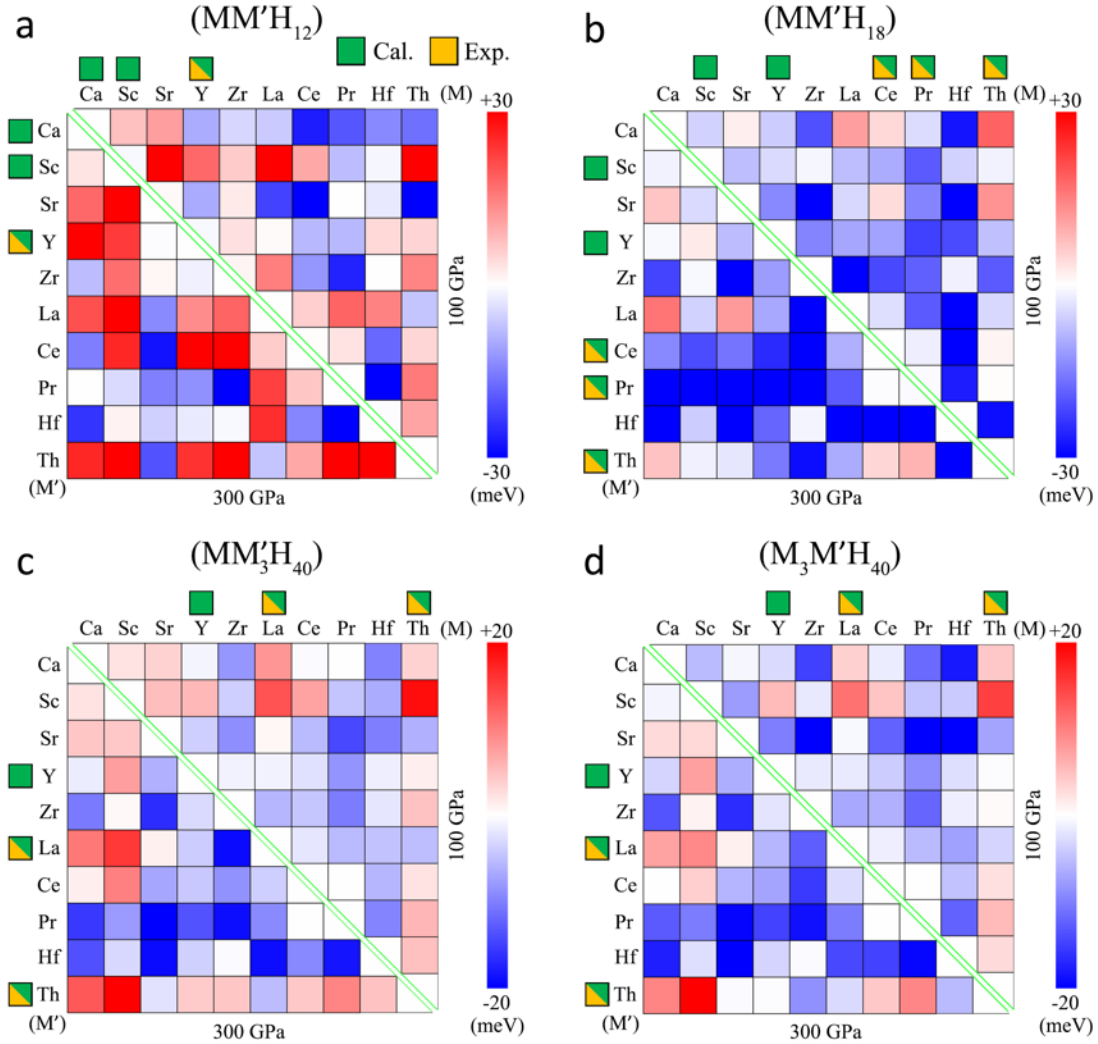


Fig. 6: The reaction enthalpies of two metal superhydrides with the same H lattice forming a mixed metal superhydrides. The formulas for calculating the reaction energies are shown in the Methods section of the text. The energies are shown in meV per atom. Negative reaction enthalpies mean the two metal superhydrides are more stable. **a**, The reaction energies of forming $MM'H_{12}$ from MH_6 and $M'H_6$. **b**, The reaction energies of forming $MM'H_{18}$ from MH_9 and $M'H_9$. **c**, The reaction energies of forming MM'_3H_{40} from MH_{10} and $M'H_{10}$. **d**, The reaction energies of forming $M_3M'H_{40}$ from MH_{10} and $M'H_{10}$.

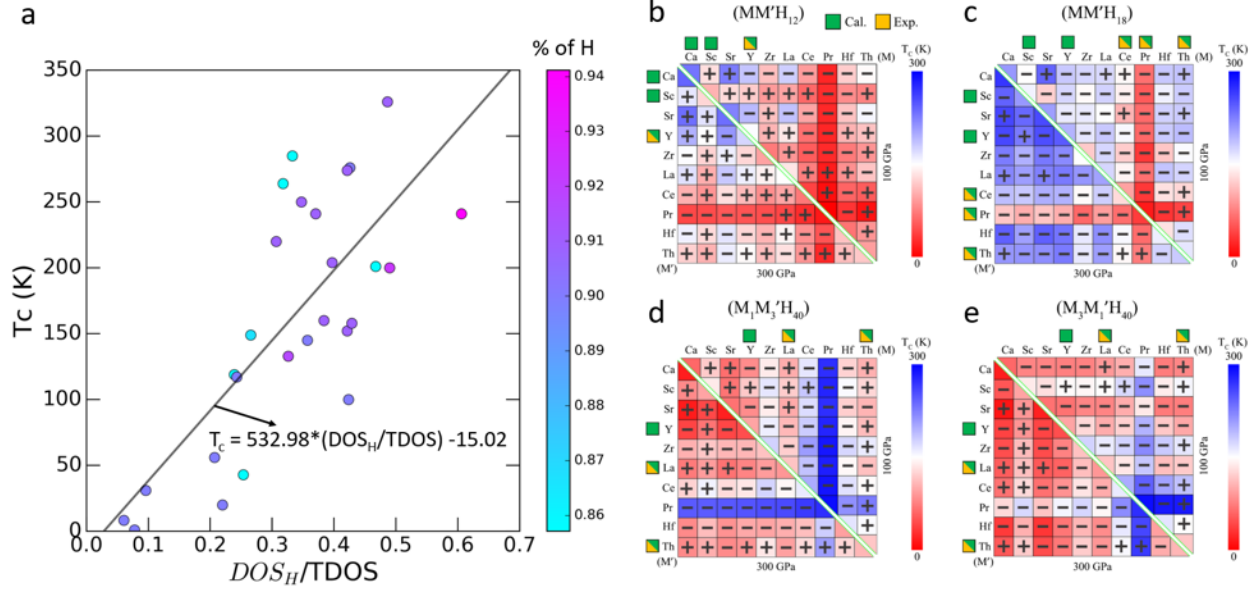


Fig. 7: Estimate T_c for mixed metal superhydrides. **a**, The relation between T_c and the ratio of density of hydrogen states (DOS_H) and total density of states (TDOS) at Fermi level of metal superhydrides predicted by DFT method. The T_c values are taken from literatures. **b – e**, The estimated T_c using calculated $DOS_H/TDOS$ at Fermi level for the conceived mixed metal superhydrides. The order of the metals and rule of combinations are kept the same as in Supplementary Fig. 6. The color shows T_c (blue represents higher T_c), whereas the + and - signs show the sign of the reaction enthalpies that are presented in Supplementary Fig. 6, *i.e.* - signs indicate that the mixed metal superhydrides are stable against the decomposition into single metal superhydrides. These results show that mixing metals in superhydrides has the potential to improve T_c by increasing the density of hydrogen related states at the Fermi level.

References

1. Peng, F. *et al.* Hydrogen Clathrate Structures in Rare Earth Hydrides at High Pressures: Possible Route to Room-Temperature Superconductivity. *Phys. Rev. Lett.* **119**, 107001 (2017).
2. Zhou, D. *et al.* Superconducting praseodymium superhydrides. *Science Advances* **6**, eaax6849 (2020).
3. Xiao, X. *et al.* Structure and superconductivity of protactinium hydrides under high pressure. *J. Phys.: Condens. Matter* **31**, 315403 (2019).
4. Wang, H., Tse, J. S., Tanaka, K., Iitaka, T. & Ma, Y. Superconductive sodalite-like clathrate calcium hydride at high pressures. *PNAS* **109**, 6463–6466 (2012).
5. Qian, S., Sheng, X., Yan, X., Chen, Y. & Song, B. Theoretical study of stability and superconductivity of ScH_n (n=4-8) at high pressure. *Phys. Rev. B* **96**, 094513 (2017).
6. Abe, K. Hydrogen-rich scandium compounds at high pressures. *Phys. Rev. B* **96**, 144108 (2017).
7. Ye, X., Zarifi, N., Zurek, E., Hoffmann, R. & Ashcroft, N. W. High Hydrides of Scandium under Pressure: Potential Superconductors. *J. Phys. Chem. C* **122**, 6298–6309 (2018).
8. Troyan, I. A. *et al.* Anomalous high-temperature superconductivity in YH₆. *arXiv:1908.01534 [cond-mat]* (2020).
9. Li, Y. *et al.* Pressure-stabilized superconductive yttrium hydrides. *Scientific Reports* **5**, 9948 (2015).
10. Semenok, D. V. *et al.* Superconductivity at 161 K in thorium hydride ThH₁₀: Synthesis and properties. *Materials Today* **33**, 36–44 (2020).
11. Li, X. *et al.* Polyhydride CeH₉ with an atomic-like hydrogen clathrate structure. *Nature Communications* **10**, 3461 (2019).
12. Salke, N. P. *et al.* Synthesis of clathrate cerium superhydride CeH₉ at 80-100 GPa with atomic hydrogen sublattice. *Nature Communications* **10**, 4453 (2019).
13. Kruglov, I. A. *et al.* Uranium polyhydrides at moderate pressures: Prediction, synthesis, and expected superconductivity. *Science Advances* **4**, eaat9776 (2018).
14. Geballe, Z. M. *et al.* Synthesis and Stability of Lanthanum Superhydrides. *Angewandte Chemie International Edition* **57**, 688–692 (2018).
15. Errea, I. *et al.* Quantum crystal structure in the 250-kelvin superconducting lanthanum hydride. *Nature* **578**, 66–69 (2020).
16. Liu, H., Naumov, I. I., Hoffmann, R., Ashcroft, N. W. & Hemley, R. J. Potential high-T_c superconducting lanthanum and yttrium hydrides at high pressure. *Proceedings of the National Academy of Sciences* **114**, 6990 (2017).
17. Somayazulu, M. *et al.* Evidence for Superconductivity above 260 K in Lanthanum Superhydride at Megabar Pressures. *Phys. Rev. Lett.* **122**, 027001 (2019).
18. Kvashnin, A. G., Semenok, D. V., Kruglov, I. A., Wrona, I. A. & Oganov, A. R. High-Temperature Superconductivity in a Th–H System under Pressure Conditions. *ACS Appl. Mater. Interfaces* **10**, 43809–43816 (2018).
19. Xie, H. *et al.* Hydrogen Pentagraphenelike Structure Stabilized by Hafnium: A High-Temperature Conventional Superconductor. *Phys. Rev. Lett.* **125**, 217001 (2020).
20. Chen, W. *et al.* Synthesis of molecular metallic barium superhydride: pseudocubic BaH₁₂. *Nature Communications* **12**, 273 (2021).
21. Kruglov, I. A. *et al.* Superconductivity of LaH₁₀ and LaH₁₆ polyhydrides. *Phys. Rev. B* **101**, 024508 (2020).
22. Hooper, J., Terpstra, T., Shamp, A. & Zurek, E. Composition and Constitution of Compressed Strontium Polyhydrides. *J. Phys. Chem. C* **118**, 6433–6447 (2014).
23. Wang, Y., Wang, H., Tse, J. S., Iitaka, T. & Ma, Y. Structural morphologies of high-pressure polymorphs of strontium hydrides. *Phys. Chem. Chem. Phys.* **17**, 19379–19385 (2015).
24. Zhang, J. *et al.* High-temperature superconductivity in the Ti–H system at high pressures. *Phys. Rev. B* **101**, 134108 (2020).
25. Semenok, D. V., Kvashnin, A. G., Kruglov, I. A. & Oganov, A. R. Actinium Hydrides AcH₁₀, AcH₁₂, and AcH₁₆ as High-Temperature Conventional Superconductors. *J. Phys. Chem. Lett.* **9**, 1920–1926 (2018).